



**CHARACTERIZATION OF ELECTROMAGNETIC  
FIELDS IN AN EXTENDED CHAMBER AT THE  
SHORT PULSE EXPERIMENTAL ELECTRON DEVICE  
(SPEED) SIMULATOR**

**Kenneth K. Hunt**

**Physitron, Inc.  
3304 Westmill Drive  
Huntsville, AL 35805**

**DTIC  
ELECTE  
JUN 01 1993  
S A D**

**April 1993**

**Final Report**

---

**APPROVED FOR PUBLIC RELEASE; DISTRIBUTION IS UNLIMITED.**

---

**93 5 28 08 5**

**93-12152**



**PHILLIPS LABORATORY  
Space and Missiles Technology Directorate  
AIR FORCE MATERIEL COMMAND  
KIRTLAND AIR FORCE BASE, NM 87117-5776**

---

PL-TR--92-1065

This final report was prepared by Physitron, Inc, Huntsville, Alabama, under Contract F29601-89-C-0014, Job Order 8809TBAA, with Phillips Laboratory, Kirtland Air Force Base, New Mexico. The Laboratory Project Officer-in-Charge was Mr William T. Kemp/VTET.

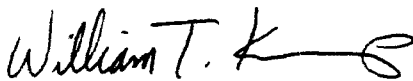
When Government drawings, specifications, or other data are used for any purpose other than in connection with a definitely Government-related procurement, the United States Government incurs no responsibility or any obligation whatsoever. The fact that the Government may have formulated or in any way supplied the said drawings, specifications, or other data, is not to be regarded by implication, or otherwise in any manner construed, as licensing the holder, or any other person or corporation; or as conveying any rights or permission to manufacture, use, or sell any patented invention that may in any way be related thereto.

This report has been authored by a contractor of the United States Government. Accordingly, the United States Government retains a nonexclusive, royalty-free license to publish or reproduce the material contained herein, or allow others to do so, for the United States Government purposes.

This report has been reviewed by the Public Affairs Office and is releasable to the National Technical Information Service (NTIS). At NTIS, it will be available to the general public, including foreign nationals.

If your address has changed, or if your organization no longer employs the addressee, please notify PL/VTET, 3550 Aberdeen SE, Kirtland AFB, NM 87117-5776, to help maintain a current mailing list.

This technical report has been reviewed and is approved for publication.



WILLIAM T. KEMP  
Project Officer



Dr. B.K. SINGARAJU, GM-15  
Chief, Electronics and  
Software Division

FOR THE COMMANDER



THOMAS M. DAVIS, Lt Col, USAF  
Acting Director of Space and Missiles  
Technology

DO NOT RETURN COPIES OF THIS REPORT UNLESS CONTRACTUAL OBLIGATIONS OR NOTICE ON A SPECIFIC DOCUMENT REQUIRES THAT IT BE RETURNED.

REPORT DOCUMENTATION PAGE			Form Approved OMB No. 0704-0188	
Public reporting burden for this collection of information is estimated to average 7 hours per response, including the time for reviewing instructions, searching existing data sources, gathering and maintaining the data needed, and completing and reviewing the collection of information. Send comments regarding this burden estimate or any other aspect of this collection of information, including suggestions for reducing this burden, to Washington Headquarters Services, Directorate for Information Operations and Reports, 1215 Jefferson Davis Highway, Suite 1204, Arlington, VA 22202-4302, and to the Office of Management and Budget, Paperwork Reduction Project (0704-0188), Washington, DC 20503.				
1. AGENCY USE ONLY (Leave blank)	2. REPORT DATE April 1993	3. REPORT TYPE AND DATES COVERED Final, May 92 - Dec 92		
4. TITLE AND SUBTITLE CHARACTERIZATION OF ELECTROMAGNETIC FIELDS IN AN EXTENDED CHAMBER AT THE SHORT PULSE EXPERIMENTAL ELECTRON DEVICE (SPEED) SIMULATOR			5. FUNDING NUMBERS C: F29601-89-C-0014 PE: 62601F PR: 8809 TA: TB WU: AA	
6. AUTHOR(S) Kenneth K. Hunt				
7. PERFORMING ORGANIZATION NAME(S) AND ADDRESS(ES) Physitron, Inc. 3304 Westmill Drive Huntsville, AL 35805			8. PERFORMING ORGANIZATION REPORT NUMBER	
9. SPONSORING / MONITORING AGENCY NAME(S) AND ADDRESS(ES) Phillips Laboratory 3550 Aberdeen Avenue, SE Kirtland AFB, NM 87117-5776			10. SPONSORING / MONITORING AGENCY REPORT NUMBER PL-TR--92-1065	
11. SUPPLEMENTARY NOTES The prime contractor was Mission Research Corp, Albuquerque, NM.				
12a. DISTRIBUTION AVAILABILITY STATEMENT Approved for public release; distribution is unlimited.			12b. DISTRIBUTION CODE	
13. ABSTRACT (Maximum 200 words)  The electromagnetic (EM) fields present during testing in a large vacuum chamber at the Short Pulse Experimental Electron Device (SPEED) facility are observed and measured using B-dot and D-dot detectors. Because the cathode of the vacuum diode is exposed to the chamber, the EM fields are significant and could adversely affect nonfaraday-shielded experiments. The differential magnetic fields and electric fields are nearly isotropically distributed, build to a maximum at 100-200 ns of $7.9 \times 10^9$ A/m-s and $9 \times 10^{10}$ V/m-s, respectively, then decay for $\sim 1000$ ns. Fourier analysis of spectra gives primary frequencies (460, 550, and 60 MHz) characteristic of the dimensions of the chamber and of electrons rebounding between the target and the pulse generators. A collimated damper is designed which should eliminate most EM fields in future tests in this configuration.				
14. SUBJECT TERMS x-ray simulator, electromagnetic (EM) fields, vacuum chamber			15. NUMBER OF PAGES 70	
			16. PRICE CODE	
17. SECURITY CLASSIFICATION OF REPORT Unclassified	18. SECURITY CLASSIFICATION OF THIS PAGE Unclassified	19. SECURITY CLASSIFICATION OF ABSTRACT Unclassified	20. LIMITATION OF ABSTRACT SAR	

## PREFACE

While the goal for this experiment was clear, the phenomenon of interest was not well understood. Flexibility was the key for both the experiment plan and execution. Success of the experiment in such a short time would not have been possible without the insight and experience of Joe Azarewicz and Leo Cotter from Physitron, Incorporated, San Diego, California, and Jake Tausch from Mission Research Corporation, Albuquerque, New Mexico.

In addition, a great deal of the success of the experiment is due to the cooperation of the Microelectronics and Photonics Research Branch, Electronics and Software Division, Space and Missiles Technology Directorate, Phillips Laboratory, Kirtland AFB, New Mexico. In particular, Bill Kemp was extremely helpful in identifying and obtaining available government equipment for this experiment.

Finally, all involved in this experiment would like to acknowledge the effort and cooperation of Rob Sharpe of Ktech Corporation, Albuquerque, New Mexico, who operated the simulator. Rob worked with the experimenters every step of the way and "went the extra mile" in keeping the simulator operating for our testing.

Accession For	
NTIS CR-81	J
DIC 1-81	11
Justification	11
By	
Distribution	
Availability Codes	
Dist	Availability or Special
A-1	

## CONTENTS

<u>Section</u>		<u>Page</u>
1.0	INTRODUCTION	1
2.0	TEST PROCEDURES	5
2.1	TEST PLAN	5
2.2	TEST SETUP	5
2.3	SENSOR DESCRIPTIONS	9
	2.3.1 Cable Currents	9
	2.3.2 Differential Magnetic Field	11
	2.3.3 Electric Field	12
3.0	TEST ANALYSIS	14
3.1	CABLE CURRENTS	14
	3.1.1 Shot 1	14
	3.1.2 Shots 5 and 6	14
	3.1.3 Results	14
3.2	MAGNETIC FIELD	14
	3.2.1 Shot 2	15
	3.2.2 Shot 3	15
	3.2.3 Shot 4	15
	3.2.4 Shot 5	15
	3.2.5 Shot 6	15
	3.2.6 Shot 9	16
	3.2.7 Results	16
3.3	ELECTRIC FIELD	17
	3.3.1 Shot 7	17
	3.3.2 Shot 8	17
	3.3.3 Results	17

## CONTENTS (Concluded)

<u>Section</u>		<u>Page</u>
3.4	SHIELDING EXPERIMENTS	18
3.4.1	Shot 6	18
3.4.2	Shot 12	18
3.4.3	Shot 13	19
3.4.4	Results	19
3.5	SHOT-TO-SHOT VARIABILITY	19
4.0	RESULTS AND CONCLUSIONS	40
	REFERENCES	43
	APPENDIX	
	EQUIPMENT	44

## FIGURES

<u>Figure</u>		<u>Page</u>
1.	The SPEED facility layout.	2
2.	The SPEED chamber options.	3
3.	Flow chart of the experiment test plan.	6
4.	The CML-X3 B-dot sensor.	8
5.	The HSD-3 D-dot sensor.	8
6.	Instrumentation system for recording free-field B-dot and D-dot data.	10
7.	Shot 1 scope photos.	21
8.	Shot 2 scope photos.	22
9.	Shot 3 scope photos.	23
10.	Shot 4 scope photos.	24
11.	Shot 5 scope photos.	25
12.	Shot 6 scope photos.	26
13.	Shot 7 scope photos.	27
14.	Shot 8 scope photos.	28
15.	Shot 9 scope photos.	29
16.	Shot 10 scope photos.	30
17.	Shot 11 scope photos.	31
18.	Shot 12 scope photos.	32
19.	Shot 13 scope photos.	33
20.	Digitized image and Fourier spectrum of the signal for shot 5.	34

## FIGURES (Concluded)

<u>Figure</u>		<u>Page</u>
21.	Digitized image and Fourier spectrum of the signal for shot 6.	35
22.	Digitized image and Fourier spectrum of the signal for shot 7.	36
23.	Digitized image and Fourier spectrum of the signal for shot 11.	37
24.	Front end of SPEED machine showing holes in anode plate that expose the cathode plate.	38
25.	Comparison of tantalum targets for shots 1-13.	39
26.	Geometry of a collimator and grounded hexagonal damper for the large SPEED chamber.	42
A-1.	Large chamber attached to the SPEED machine.	45
A-2.	Camera-equipped oscilloscopes in the shield room.	45
A-3.	The D- and B-dot sensors mounted on an aluminum box in the chamber.	46

## TABLES

<u>Table</u>		<u>Page</u>
1.	Experiment record by shot.	7
2.	Specifications for the CML-X3 B-dot sensor.	12
3.	Specifications for the HSD-3 and ACD-4B D-dot sensors.	13

## 1.0 INTRODUCTION

This report summarizes the results of a study to observe and measure the electromagnetic (EM) fields and cable currents that are present during testing of unshielded experiments in a large chamber at the Short Pulse Experimental Electron Device (SPEED) facility operated by the Ktech Corporation in Albuquerque, New Mexico. Conclusions include recommendations for mitigation of such fields and currents during x-ray testing.

The SPEED simulator is of interest because of its proximity and unique fast-rise-time, low-energy x-ray capability which could make it the closest spectral match of any of the large above-ground test (AGT) simulators for certain survivability requirements. The SPEED is a variable energy-pulsed e-beam accelerator with an x-ray converter. Using a debris shield and bremsstrahlung converter to produce x rays with adjustable end-point energies, SPEED provides an energy source with good spectral and temporal fidelity for transient radiation effects on electronics (TREE), dose enhancement, internal electromagnetic pulse (IEMP), and system generated electromagnetic pulse (SGEMP) studies. With a particle energy range of 0.15–1.3 MeV, a rise time <10 ns, and an optimal fluence of  $2 \times 10^{12}$  rad(Si)/s, SPEED is suited to studies where a low-energy spectrum is appropriate.

The layout of the SPEED facility is shown in Figure 1. Experiment setup options are shown in Figure 2. For vacuum-level testing of experiments larger than a few inches, a cylindrical aluminum extension is available, providing a test chamber ~120-cm long and 90 cm in diameter (Fig. 2a). Samples can be mounted in the chamber on an adjustable Plexiglas table for electrical isolation. Connections to the outside are made through grounded vacuum BNC feedthrough connectors at the rear of the chamber, then through double-shielded cables to the shield room.

Previous x-ray testing using the extended chamber has shown that unshielded experiments (not faraday caged) can experience unexpected part failures. When the experiments are faraday shielded, they show no degradation. It has been postulated that such failures are caused by EM interference and not by the x rays. The chamber has been monitored on one occasion with a 2-cm-diam. coil which easily detected a differential magnetic (H) field (suggesting an accompanying electric [E] field), but

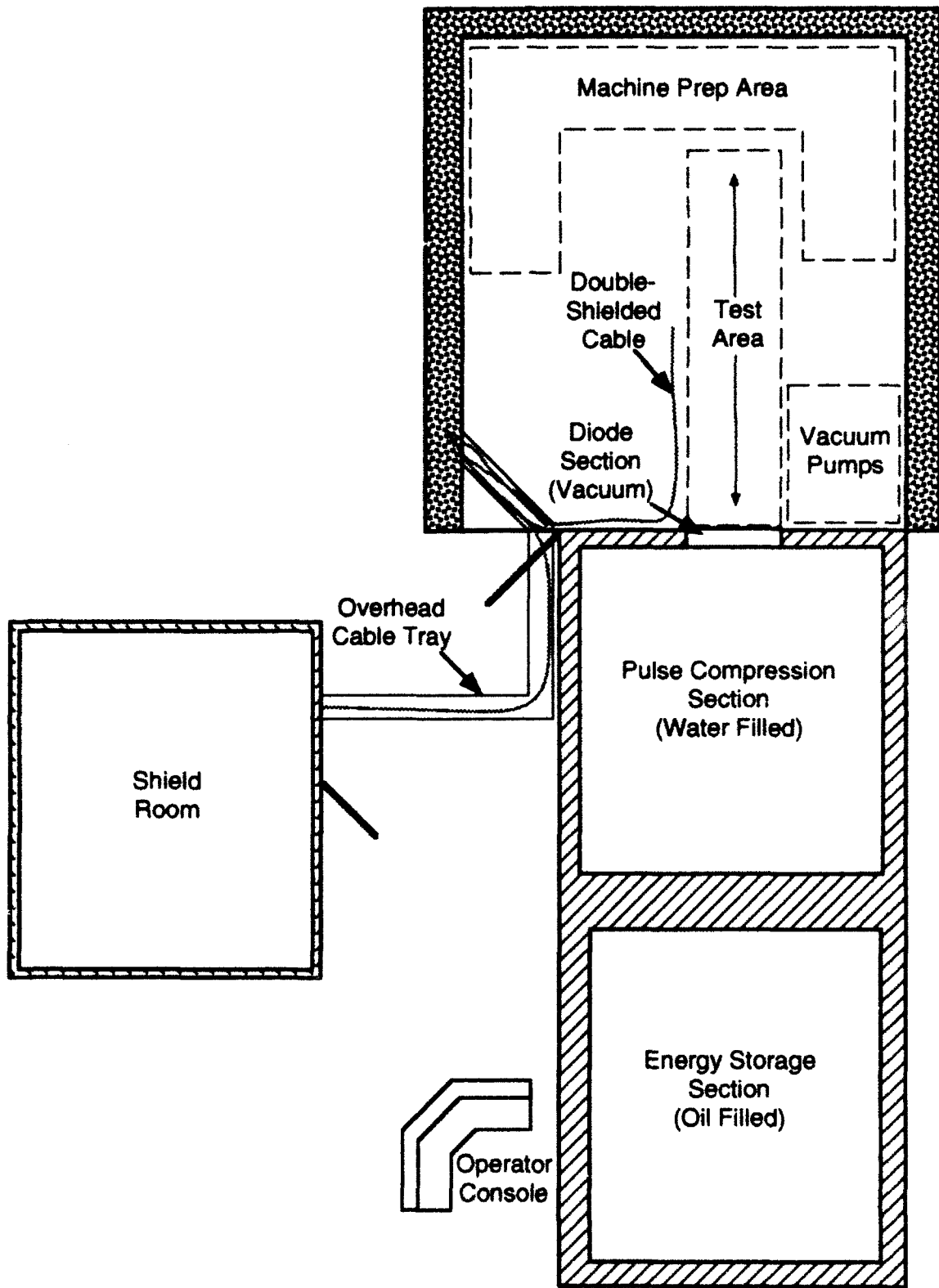
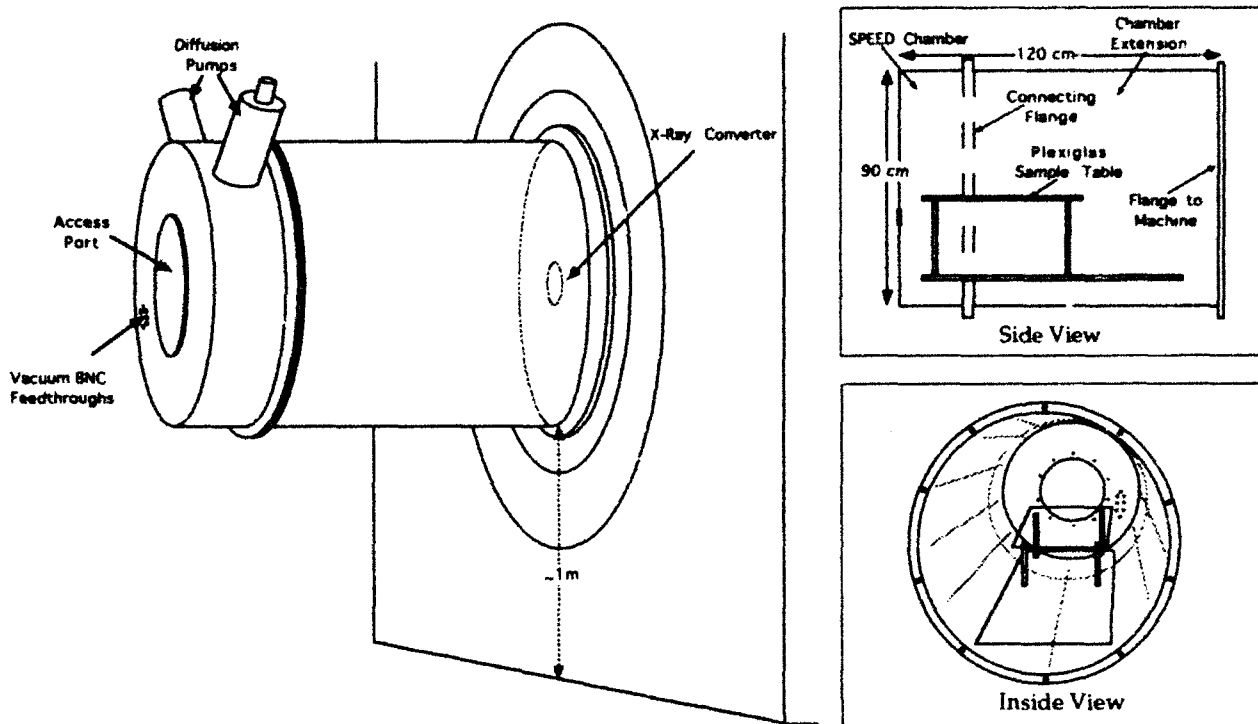
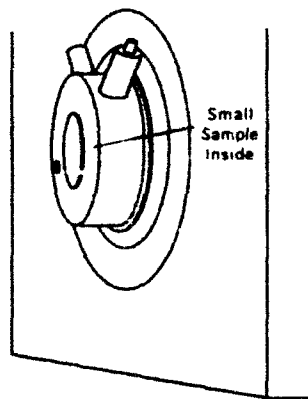


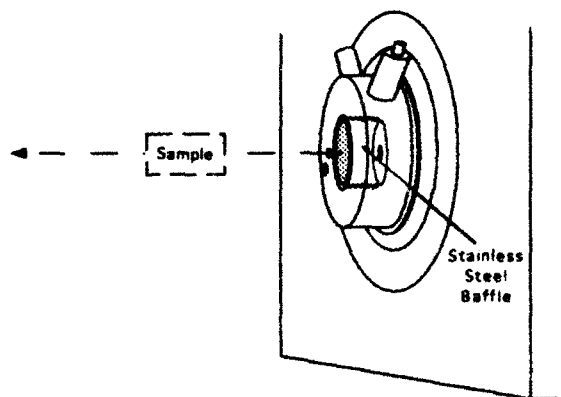
Figure 1. The SPEED facility layout.



(a) Larger or lower dose rate samples requiring vacuum.



(b) Small samples under vacuum at high dose rates.



(c) Larger samples not requiring vacuum.

Figure 2. The SPEED chamber options.

magnitude and duration were not measured. While this test tended to support the theory of a potentially damaging EM artifact, there was still some doubt that failure of unshielded experiments was due to that testing anomaly until the fields in the chamber could be quantified.

## 2.0 TEST PROCEDURES

### 2.1 TEST PLAN

It was initially assumed that the SPEED simulator would produce EM fields for unshielded experiments since the simulator diode target was not shielded against such emanations during the test. Because few experiments had been configured to be sensitive to such fields, very little information was available about their amplitude, frequency, or duration. This led to the development of a flexible test plan which would allow the measurement of the electric and magnetic components of the expected EM pulse but could be modified depending on intermediate results. A flow chart of the test plan is shown in Figure 3. The test plan was designed to:

- Measure the signal noise outside, and cable currents inside, the chamber. Both were expected to be insignificant for short cable lengths and low-energy x-ray spectra.
- Record the differential E- and H-fields present to quantitatively determine the magnitude, duration, and bandwidth of such fields.
- Try possible techniques to mitigate the EM fields.

### 2.2 TEST SETUP

A total of 3 days of SPEED test time was available for the experiment. Government-furnished equipment (sensors, oscilloscopes, scope cameras) was adequate to measure and quantify expected fields and cable currents.

Three camera-equipped oscilloscopes were located in an adjacent shield room (Fig. 1) and were used to record sensor signals. In general, testing included the following steps:

1. Sensors (Subsection 2.3) were placed on the insulated sample platform in the chamber extension (Fig. 2a) to maximize possible EM effects.

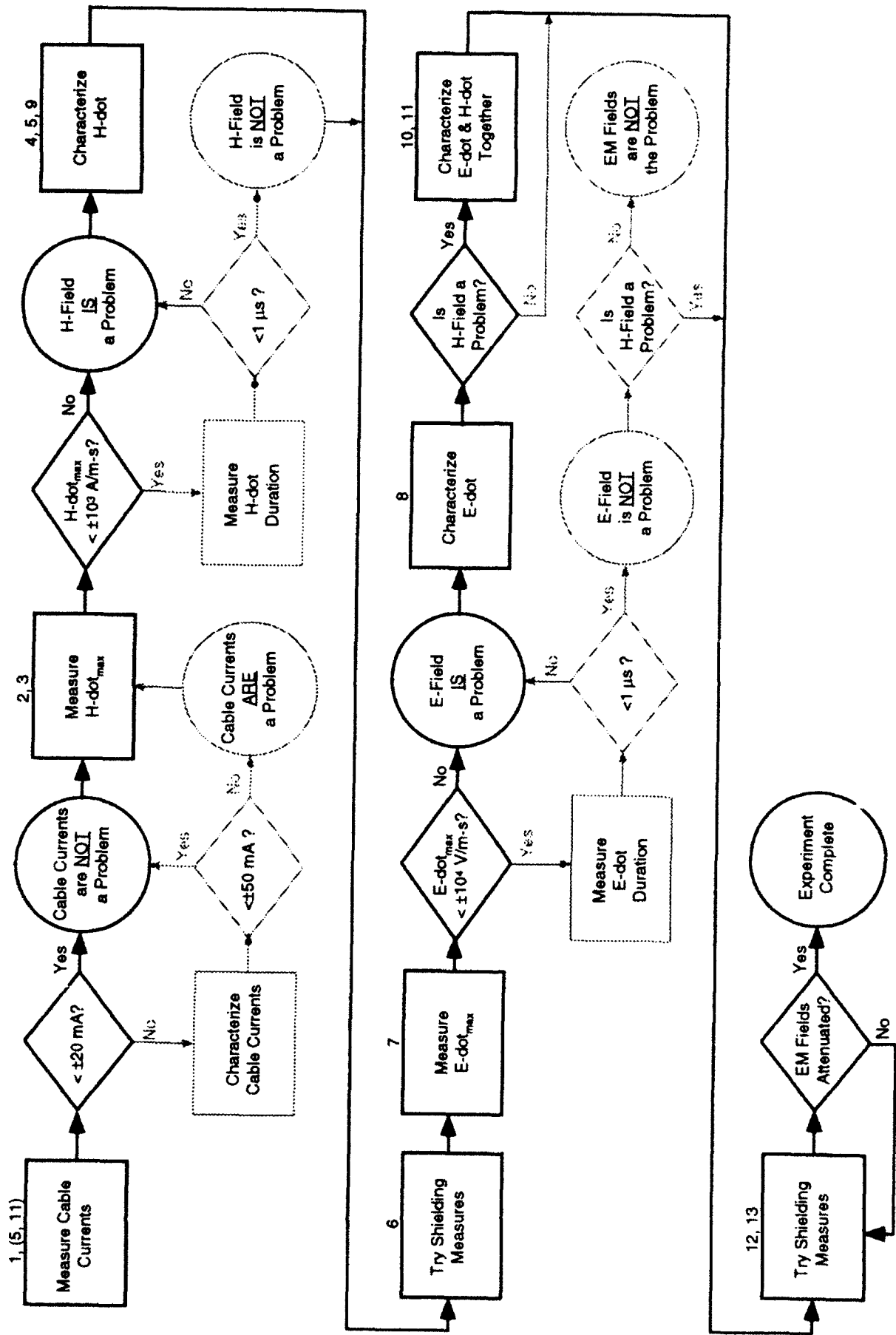


Figure 3. Flow chart of the experiment test plan. The actual progress of the experiment is shown in solid lines, starting in the upper left corner. Numbers above the blocks indicate the SPEED shots described in Table 1.

Table 1. Experiment record by shot.

Shot	Description	Purpose	Expected Results	Results
1	1-m RG-58 cable inside chamber (50 $\Omega$ termination).	Cable current check.	Unknown.	Cable current <6 mA.
2	50 $\Omega$ termination at outside chamber BNC.	Noise check.	Signal - amplitude unknown.	Noise <6 mA.
3	2 B-dot sensors ( $\theta = 0^\circ$ , $\theta = 90^\circ$ ), rear of chamber. <sup>a</sup>	First H-field check.	Improved signal images. Differences between sensors.	Signal detected, but need more gain.
4	Same as 2.	Improved H-field check.	Improved signal images.	Better signals recorded; need more gain, faster sweep.
5	1 B-dot sensor, $\theta = 0^\circ$ , rear of chamber. <sup>a</sup>	Improved H-field check.	Improved signal images.	Differences between $\theta$ minor.
6	Same as 4 except centered in chamber. Same as 1 (cable current check).	Improved H-field check. Improved cable current check.	Improved signal images.	Good frequency image at 10 ns. Signal rings for >500 ns.
7	Same as 5 except aluminum plate cover over diode target. <sup>b</sup>	Attempt to attenuate EM fields.	Significant attenuation.	Quantifiable images. Max cable current = 5 mA.
8	2 D-dot sensors, centered.	First E-field check.	Signals - amplitudes unknown.	No attenuation.
9	D-dot sensor, $\theta = 45^\circ$ , rear. <sup>a</sup>	Improved E-field check.	Improved signal images.	Good signals recorded. Less scope gain needed. S3 did not trigger.
10	Same as 7.	Check for B-dot cable grounding problems.	No significant differences.	Quantifiable images.
11	2 B-dot sensors (cables floating, rounded), $\theta = 0^\circ$ , centered in chamber. <sup>a</sup>	Compare H- and E-fields. Look for end of ringing.	ences.	No significant differences.
12	- and D-dot sensors (both $\theta = 0^\circ$ ). <sup>a</sup>	Improved comparison.	Unknown.	Good images for comparison. Signals die away after 1.2 $\mu$ s.
13	Same as 10.	Attempt to attenuate EM fields.	Improved signal images.	Improved images.
14	Same as 11 except screen added at front of chamber.	Attempt to attenuate EM fields.	Significant attenuation.	Minor attenuation.
15	D- and B-dot sensors placed in faraday box (50 $\Omega$ terminator at box also).	Attempt to attenuate EM field.	Complete attenuation of E-field. Slight attenuation of H-field.	Complete attenuation of E-field. Some attenuation of H-field.

NOTES

<sup>a</sup>Refer to Figures 4 and 5 (insets).

<sup>b</sup>Since the effect was minimal, the aluminum plate used on shot 6 was left in place for shots 7-13.

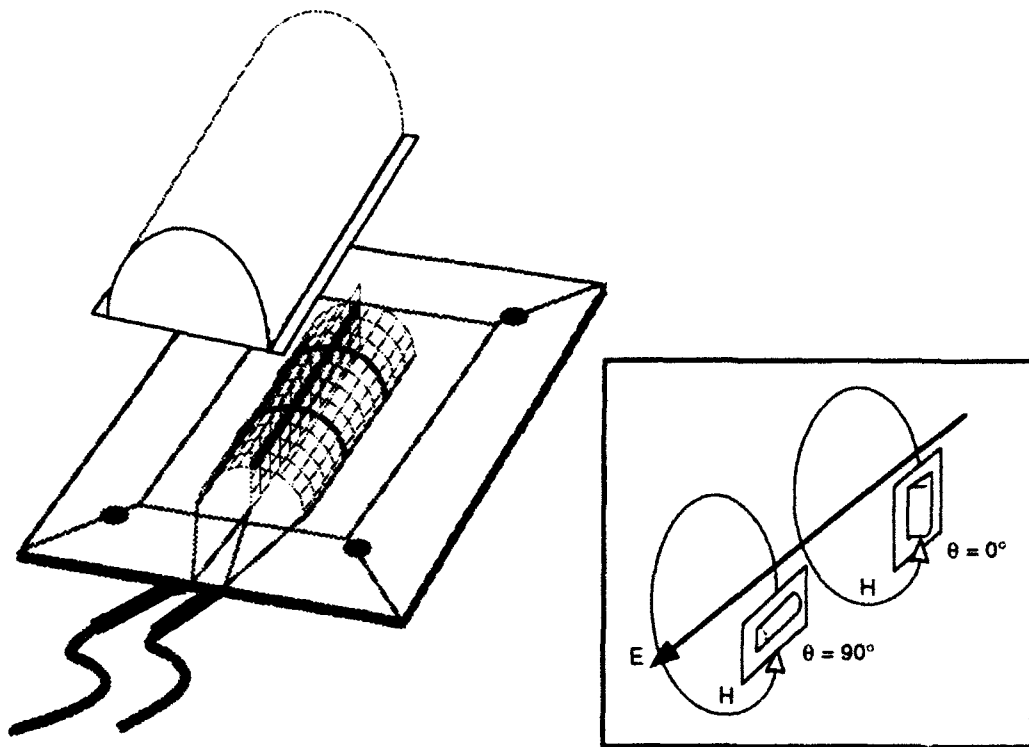


Figure 4. The CML-X3 B-dot sensor. Insert shows sensor orientation for maximum ( $\theta = 0^\circ$ ) and minimum ( $\theta = 90^\circ$ ) sensor response to the magnetic field from the initial pulse.

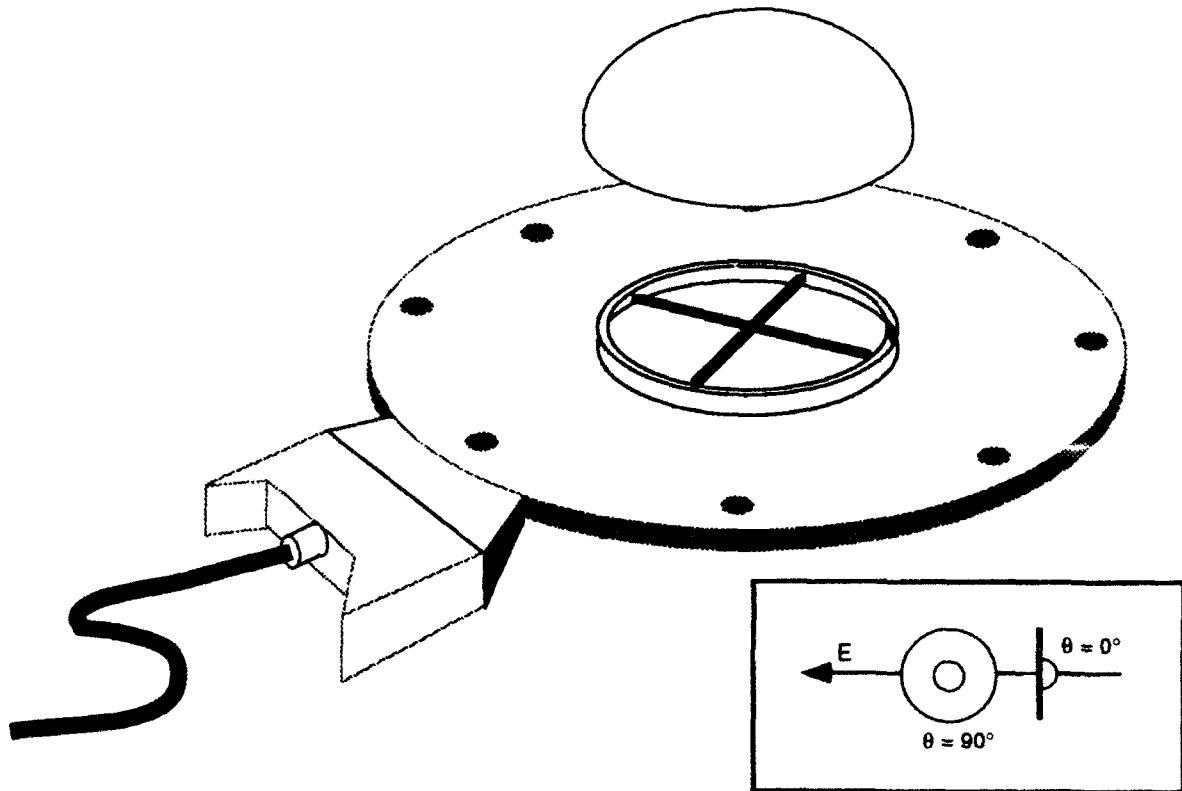


Figure 5. The HSD-3 D-dot sensor. Insert shows sensor orientation for maximum ( $\theta = 0^\circ$ ) and minimum ( $\theta = 90^\circ$ ) sensor response to the initial pulse.

2. The SPEED simulator was tuned (through target diode preparation and peak voltage) to produce the lowest energy x-ray pulse available to minimize radiation effects and duplicate test conditions for previous tests in the extended chamber.
3. At shot time, a trigger signal for all oscilloscopes was obtained from the SPEED vacuum voltage monitor (VVM). It was delayed by ~70 ns due to cable length.
4. Sensor signals were transmitted with ~80-ns delays through the double-shielded SPEED cables to the camera-equipped oscilloscopes (differences in signal and trigger delays gave prerad traces on shot photos).
5. Scope cameras recorded sensors signals on Polaroid film.
6. Experimenters reviewed the photographic evidence and made changes to sensors (type, position, orientation, shielding) or oscilloscopes settings (time scale, signal amplitude) for the next test, and the cycle was repeated.

Table 1 lists the shot record for the full experiment. Using steps 1-6, the test plan was executed as shown in solid lines in Figure 3. Shot numbers are shown above the appropriate "action" blocks and can be cross referenced to Table 1. Figure 6 shows a diagram of a typical instrumentation system – in this case, the setup used for shots 10–13.

## 2.3 SENSOR DESCRIPTIONS

As shown in Table 1, the interior of the chamber was monitored for cable currents, differential magnetic fields, and electric fields.

### 2.3.1 Cable Currents

Cable currents were observed and measured using a 1-m length of RG-58 coaxial cable terminated with  $50 \Omega$  ( $R_C$ ). The cable was laid on the Plexiglas table, generally perpendicular to the axis of the chamber.

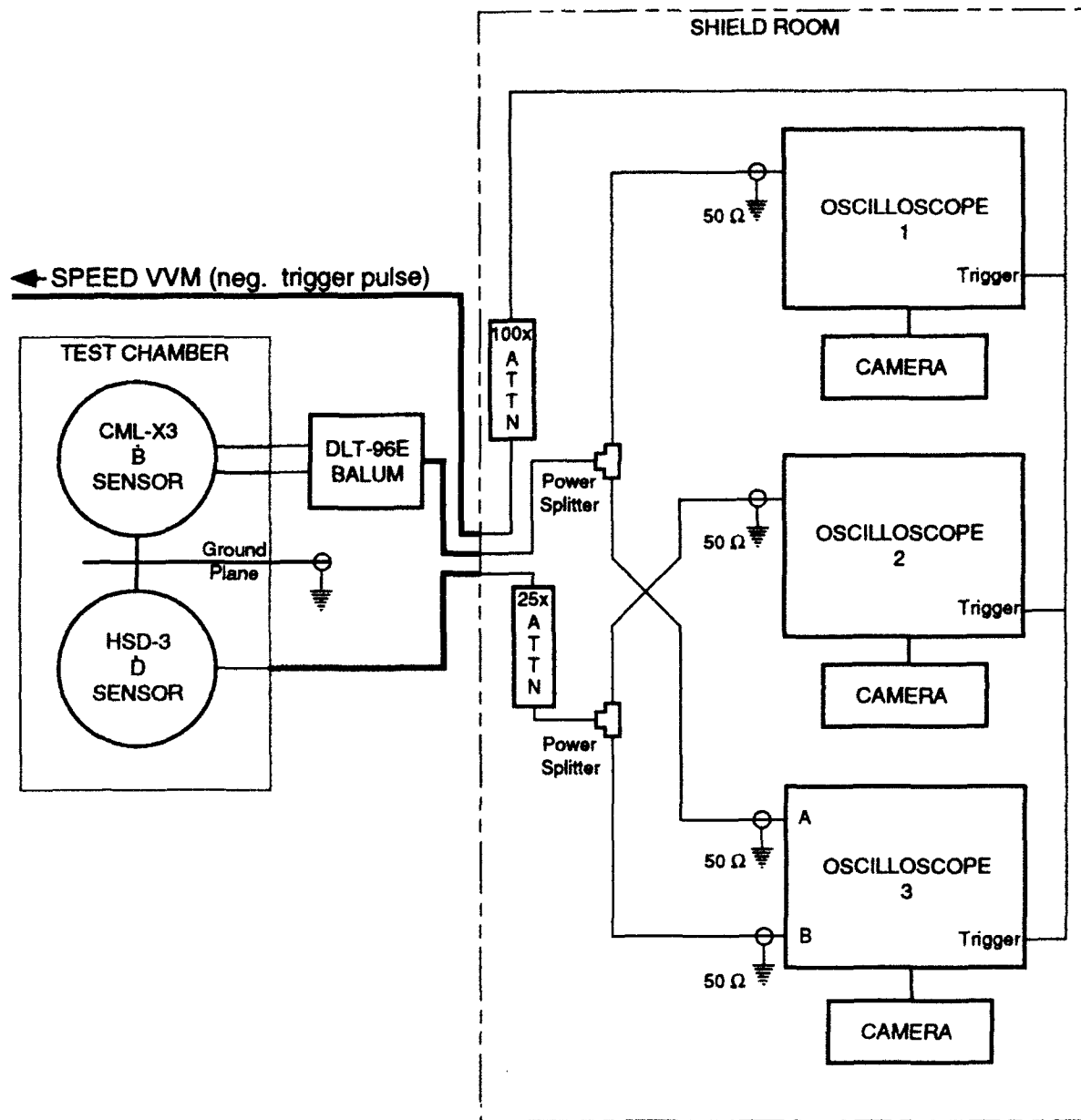


Figure 6. Instrumentation system for recording free-field B-dot and D-dot data.

### 2.3.2 Differential Magnetic Field

Signals were detected with the CML-X3 B-dot sensor (shown in Fig. 4, specifications in Table 2) through the DLT-96E balun. The cylindrical moebius loop sensor is a small radiation-hardened half-cylinder loop mounted on a conducting surface to measure the time rate of change of the magnetic flux density ( $\text{dB}/\text{dt}$  or B-dot, given in tesla/second). The voltage signal developed across the gap in the equivalent cylindrical loop by the changing H-field is sensed in the differential mode. The moebius configuration and the differential output provide for common mode rejection of unwanted signals generated in the cables by radiation and E-field components. This rejection takes place by subtracting the positive and negative signals through the balun. (The balun was certified to attenuate the signal by 6 dB up to 250 MHz; higher frequencies would be attenuated more.) Since

$$\frac{d\vec{H}}{dt} = \frac{d\vec{B}/dt}{\mu_0}$$

and

$$V_o = \frac{dB}{dt} A_{eq} \cos\theta$$

then

$$\frac{dH}{dt} = \frac{V_o}{A_{eq} \mu_0 \cos\theta} \quad (\text{in amperes/meter-second}) \quad (1)$$

where  $V_o$  is the sensor output voltage,  $A_{eq}$  is the sensor equivalent area (in square meters),  $\mu_0$  is the permeability of free space ( $4\pi \times 10^{-7}$  H/m), and  $\theta$  is the angle between the B-field and a vector normal to the sensor ground plane.

The following summarizes the variations attempted:

- Sensors were oriented so that the initial H-field would be maximized ( $\theta = 0^\circ$ ) and minimized ( $\theta = 90^\circ$ ) on the same shot (Fig. 5 inset); after determining that only minor differences existed, further testing used  $\theta = 0^\circ$ .

- Sensors were placed on the center line of the chamber, both near the back and near the center.
- Grounding of the semirigid sensor cables was varied from free-floating (touching the chamber only at the BNC feedthrough) to totally grounded (touching the chamber along the entire length of the cable).

Table 2. Specifications for the CML-X3 B-dot sensor.

Parameter	
$A_{eq}$	$5 \times 10^{-4} \text{ m}^2$
Frequency Response (3-dB pt)	700 MHz
Risetime	0.5 ns
Maximum Output	1.5 kV peak
Maximum Field Change	$3 \times 10^6 \text{ T/s}$
Radiation Dose Rate	
X ray (<20 keV)	$10^{13} \text{ rad/s}$
$\gamma$ ray (~5 MeV)	$10^{11} \text{ rad/s}$
Output Connector	2 5-m semirigid cables, OSM-210-1 (50 $\Omega$ )

### 2.3.3 Electric Field

Signals were detected using an HSD-3 D-dot sensor (Fig. 5, specifications in Table 3) which is a hollow spherical dipole sensor mounted on a conducting surface. In addition, some tests also included an ACD-4B D-dot sensor (specifications in Table 3), which is a free-field asymptotic conical dipole sensor extending the upper frequency limit for the same value of equivalent area as the HSD design.

Both sensors (but primarily the HSD-3) were used to measure the normal component of the electric displacement current ( $dD/dt$  or D-dot, given in coulombs/square meter-second) in order to calculate the differential E-field. Since

$$\frac{d\vec{E}}{dt} = \frac{d\vec{D}}{dt} \frac{1}{\epsilon_0}$$

and

$$V_o = R A_{eq} \frac{dD}{dt} \cos \theta$$

then

$$\frac{dE}{dt} = \frac{V_o}{R A_{eq} \epsilon_0 \cos \theta} \quad (\text{in volts/meter-second}), \quad (2)$$

where

- $V_o$  = the sensor output voltage
- $R$  = the sensor characteristic load impedance (50  $\Omega$ )
- $A_{eq}$  = the sensor equivalent area (in square meters)
- $\epsilon_0$  = the permittivity of free space ( $8.85 \times 10^{-12}$  F/m)
- $\theta$  = the angle between the E-field and a vector normal to the sensor ground plane

Table 3. Specifications for the HSD-3 and ACD-4B D-dot sensors.

Parameter	HSD-3	ACD-4B
$A_{eq}$	$1 \times 10^{-2} \text{ m}^2$	$1 \times 10^{-2} \text{ m}^2$
Frequency Response (3-dB pt)	$\geq 150 \text{ MHz}$	$> 1.0 \text{ GHz}$
Risetime ( $T_r$ 10-90)	$\leq 2.3 \text{ ns}$	$< 0.33 \text{ ns}$
Maximum Output	5 kV	2 kV
Output Connector	GR-874L (50 $\Omega$ )	TCC (100 $\Omega$ )

### 3.0 TEST ANALYSIS

All oscilloscope photographs taken during testing are shown in Figures 7-19. Refer to Table 1 for additional details for each shot.

#### 3.1 CABLE CURRENTS

##### 3.1.1 Shot 1

Cable currents ( $I_c$ ) were initially monitored out to 100 ns (Fig. 7a). Scope gain was set low to protect equipment against an unknown signal. The signal was near the limit of detection.

##### 3.1.2 Shots 5 and 6

Time permitted a further check of cable currents on shots 5 (Fig. 11c, lower trace) and 6 (Fig. 12c, lower trace). Using higher scope gain, the signal was recorded more accurately out to 500 ns.

##### 3.1.3 Results

Recorded voltage ( $V_r$ ) from shot 1 was estimated to be  $<0.3$  V. Since the impedance was  $50 \Omega$ ,  $I_c < 6$  mA. This was considered to be insignificant, and testing proceeded to quantify the differential H- and E-fields. For shots 5 and 6,  $V_r$  was  $<50$  mV for 75 ns, then rapidly increased to 250 mV. It rang with a characteristic frequency of 120 MHz for 300 ns, gradually diminishing to 50 mV. For

$$V_r (\text{max}) = 250 \text{ mV/m} \quad (\text{at } 75 \text{ ns})$$

$$I_c (\text{max}) = 5 \text{ mA/m}$$

#### 3.2 MAGNETIC FIELD

Shots 2-6 (Figs. 8-12) and 9 (Fig. 15) were used to observe and measure the H-field in the chamber. Shots 10-13 (Figs. 16-19) included B- and D-dot sensors for comparison.

### 3.2.1 Shot 2

Two B-dot sensors were mounted on an aluminum box, oriented such that  $\theta = 0^\circ$  and  $\theta = 90^\circ$ . The box was placed on the Plexiglas stand on the center line of the chamber, 100 cm from the face. Attenuation and gain were purposely set to protect the recording electronics since the magnitude of the signal was unknown.

### 3.2.2 Shot 3

After adjusting oscilloscope gain and in-line attenuation, it was demonstrated that (1) the long-duration ringing dominated the signal, and (2)  $\theta = 90^\circ$  provided no additional useful information over that gained by monitoring at  $\theta = 0^\circ$ . All further H-field measurements were made with one or more B-dot sensors oriented such that  $\theta = 0^\circ$ .

### 3.2.3 Shot 4

The signal from a single sensor was split twice using normal T-type splitters; therefore, quantification of the amplitudes at each scope was approximate. This shot provided a first look at the structure of the early-time ringing and was the first time the third scope was used (picture quality was poor but useful).

### 3.2.4 Shot 5

Beginning with this shot, the aluminum box was placed near the center point of the chamber, 70 cm from the face. The signal from a single sensor was split using 6-dB splitters, permitting quantification of signals.

### 3.2.5 Shot 6

As an initial attempt to attenuate the EM fields, an aluminum plate was placed over the SPEED target as described in Subsection 3.4.1. The shot was monitored with D-dot sensors, and recording settings remained the same as shot 5.

### 3.2.6 Shot 9

Since the B-dot sensors had two 5-m, semirigid signal leads, there was some concern that the positioning and grounding of those leads were affecting the output signal in the chamber. Two sensors were mounted identically except that the leads for one sensor were not allowed to touch the chamber wall and the leads for the other detector were grounded as completely as possible to the chamber wall. Signals from the two sensors gave essentially identical amplitudes and frequencies.

### 3.2.7 Results

3.2.7.1 Magnitude of Signal. The most accurate measurement of the maximum amplitude of the H-field signal is shown in Figure 11, where the peak recorded voltage was

$$V_r(\text{max}) = 1.2 \text{ V}$$

Then

$$V_o(\text{max}) = \alpha V_r(\text{max}) = 4.8 \text{ V}$$

since  $\alpha$  is the total attenuation, a product of the in-line attenuation, signal splitting, and balun attenuation (values of 1, 2, and 2, respectively, for this scope and shot).

From Equation 1,

$$\begin{aligned} \frac{dH}{dt}(\text{max}) &= \frac{V_o(\text{max})}{A_{\text{eq}} \mu_o \cos \theta} \\ &= \frac{4.8}{(5 \times 10^{-4})(4\pi \times 10^{-7})(1)} \\ &= 7.6 \times 10^9 \text{ A/m-s} \end{aligned}$$

3.2.7.2 Characteristic Frequencies. Fourier analysis was performed on digitized images of Figures 11a and 12a. The resulting plots are shown in Figures 20 and 21.

Both showed clear peaks at 450, 520, and 550 MHz. These correspond to resonant wavelengths of 65, 57, and 54 cm, respectively.

### 3.3 ELECTRIC FIELD

Shots 7 and 8 (Figs. 13 and 14) were used to observe and measure the E-field in the chamber. Shots 10–13 (Figs. 16–19) included B- and D-dot sensors for comparison.

#### 3.3.1 Shot 7

Two D-dot sensors were mounted on the aluminum box (so that  $\theta = 0^\circ$  and  $\theta = 90^\circ$ ) which was placed on the Plexiglas stand in the center of the chamber, 70 cm from the face.

#### 3.3.2 Shot 8

The sensors were unchanged from shot 7. Gains were adjusted, and a quantifiable signal was obtained.

#### 3.3.3 Results

3.3.3.1 Magnitude of Signal. The most accurate measurement of the maximum amplitude of the E-field signal is shown in Figure 14, where the peak recorded voltage was

$$V_r(\max) = 1.6 \text{ V}$$

Then

$$V_o(\max) = \alpha V_r(\max) = 40 \text{ V}$$

since  $\alpha$  is the total attenuation which is a product of the in-line attenuation and signal splitting (values of 25 and 1, respectively, for this scope and shot). From Equation 2,

$$\begin{aligned}
 \frac{dE}{dt}(\max) &= \frac{V_o(\max)}{R A_{eq} \epsilon_o \cos\theta} \\
 &= \frac{40}{(50)(1 \times 10^{-2})(8.85 \times 10^{-12})(1)} \\
 &= 9.0 \times 10^{10} \text{ V/m-s}
 \end{aligned}$$

3.3.3.2 Characteristic Frequencies. Fourier analysis was performed on digitized images of Figures 13a and 17a. The resulting plots are shown in Figures 22 and 23. Peaks at 430 and 550 MHz, corresponding to resonant wavelengths of 65 and 54 cm, respectively, are similar to the H-field results. In addition, the peak at 60 MHz is real and dominates after 80 ns (most apparent in Fig. 14 at a frequency of 17 ns). This corresponds to a wavelength of 5 m and represents the ringing of the residual electrons back and forth along the water dielectric pulse-forming lines.

#### 3.4 SHIELDING EXPERIMENTS

Three attempts were made to shield against the EM fields.

##### 3.4.1 Shot 6

It was initially assumed that the EM signal was generated by the tantalum target, even though a 3-mm carbon plate provided apparent conductive shielding; therefore, a 2-mm aluminum plate was placed over the target assembly for shot 6. Subsequent shots included the plate as part of the target.

##### 3.4.2 Shot 12

A crude shield, constructed from stainless steel screen wrapped around a copper tube, was wedged in the front of the chamber. This provided a simple test devised to cover the holes in the exposed end of the SPEED machine (Fig. 24).

### 3.4.3 Shot 13

As a final test, D- and B-dot sensors were enclosed in an aluminum box. Current on the box (with a 50- $\Omega$  terminator attached to a BNC feedthrough) was also monitored.

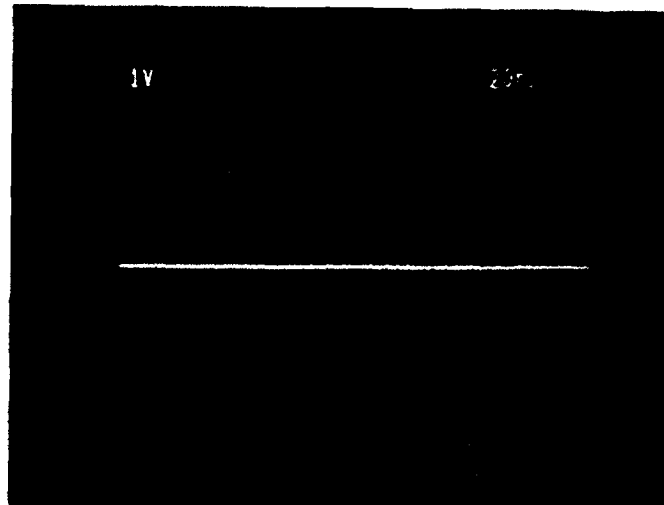
### 3.4.4 Results

Examination of the SPEED diode section (Fig. 24) revealed that the cathode plate, located ~2 cm behind the anode, is exposed around the perimeter of the circular anode plate through 3-cm-diam. holes to permit pump down of the diode assembly. The cathode is charged to 150 kV and discharges in <100 ns. There is little doubt that these holes are the source of both an E-field and free electrons during, and for long periods after, a shot. Therefore, it was anticipated that the 2-mm-thick aluminum plate over the target on shot 6 would have no apparent effect on the fields distinguishable from other machine variables. Results using the crude screen assembly (shot 12) showed some reduction in both the E- and H-fields (comparing Figs. 17 and 18). As expected, the E-field was eliminated completely inside the aluminum box (shot 13, Fig. 19a). Outside, the box acted as an antenna, so box currents were significant (Fig. 19b). Finally, since a nonferrous material was used for the box, the H-field was only slightly attenuated (Fig. 19c, lower trace).

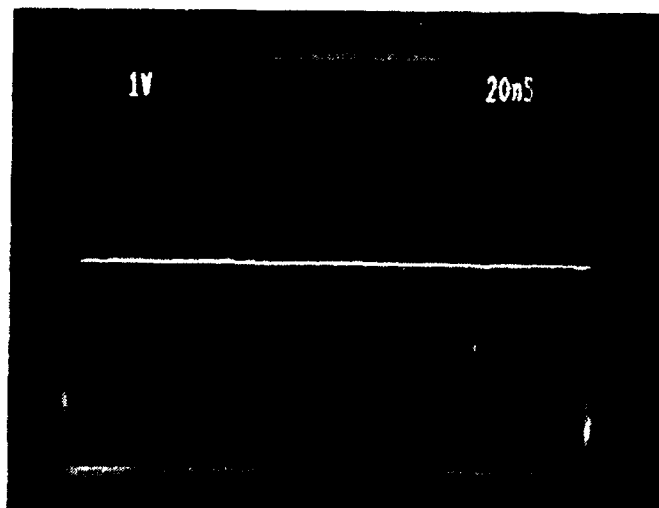
## 3.5 SHOT-TO-SHOT VARIABILITY

Quantification of results for this experiment are approximate due to the variability of the signal from the SPEED simulator as shown in the scope photos (Figs. 7-19). Since no measure was taken of the x-ray pulse being produced, the best qualitative indicator of shot-to-shot variability is shown in the damage to the tantalum targets as illustrated in Figure 25. Ideally, all should look like targets 9 and 12, where two concentric rings of tantalum were evaporated. All other targets showed incomplete formation of the rings, usually due to arcing of the diode assembly; yet from experience the machine operator indicated that all targets were indicative of acceptable machine firings and should have produced the expected x-ray fluence and spectra.

Another variability was that the ringing of the signal began before the triggering of the pulse on some shots (detected by  $D$ -dot detectors as shown in Figs. 13, 14, and 16a and by the aluminum box current monitor as shown in Fig. 19b). A possible explanation is that E-fields created in either the energy storage section or pulse compression section are sometimes transmitted to the chamber prior to the creation of the x-ray pulse.

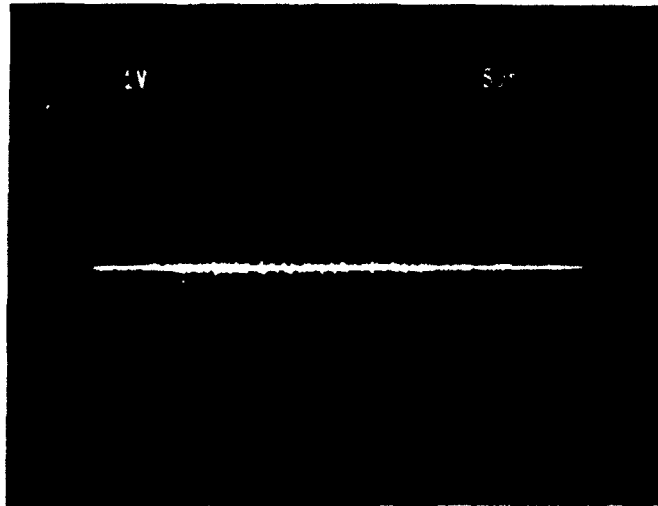


(a) Scope 1, RG-58 coaxial cable (1 m) with 50- $\Omega$  terminator.

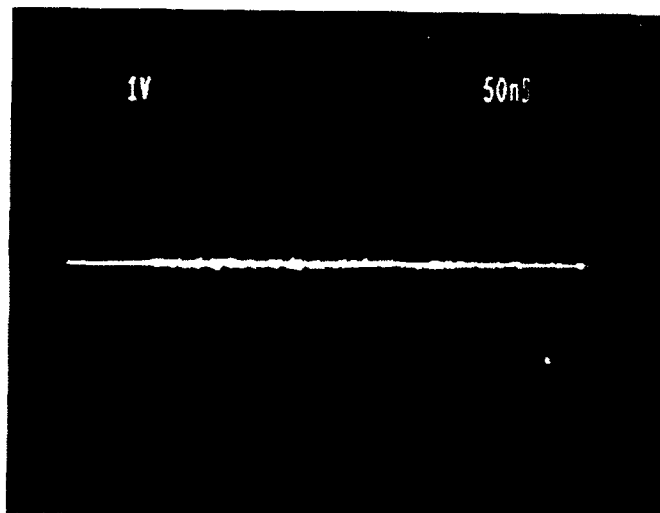


(b) Scope 2, 50- $\Omega$  terminator at BNC connector outside chamber.

Figure 7. Shot 1 scope photos. In-line attenuation at scope - 25

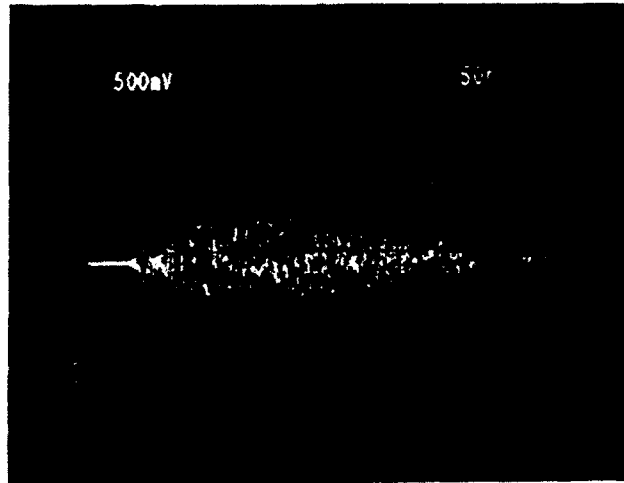


(a) Scope 1, B-dot sensor, 100 cm from front, on center line,  $\theta = 0^\circ$ .

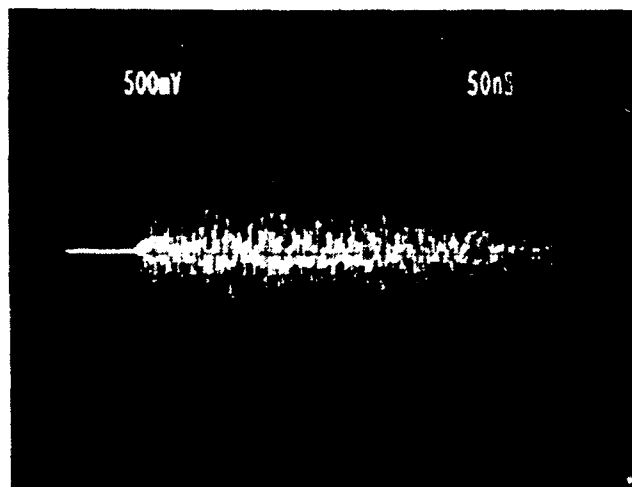


(b) Scope 2, B-dot sensor, 100 cm from front, on center line,  $\theta = 90^\circ$ .

Figure 8. Shot 2 scope photos. In-line attenuation - 25, balun attenuation - 2.

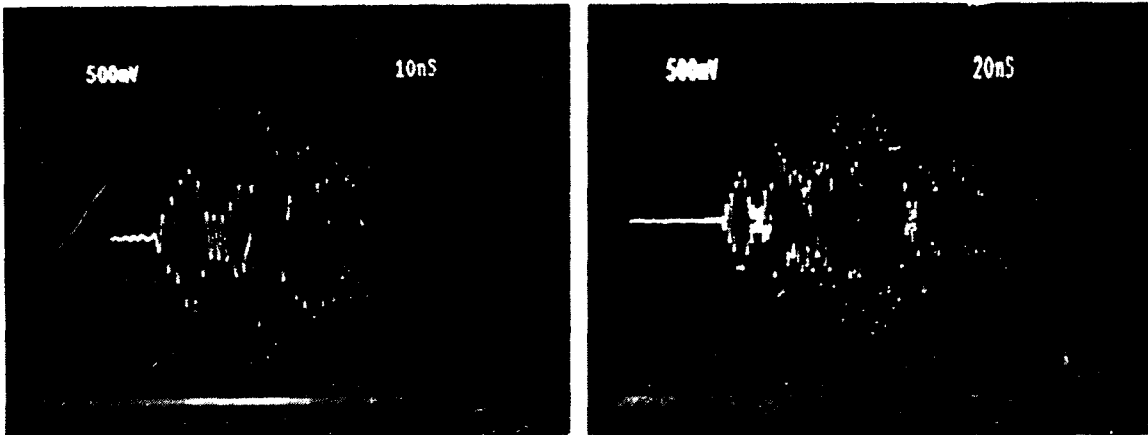


(a) Scope 1, B-dot sensor, 100 cm from front, on center line,  $\theta = 0^\circ$ .



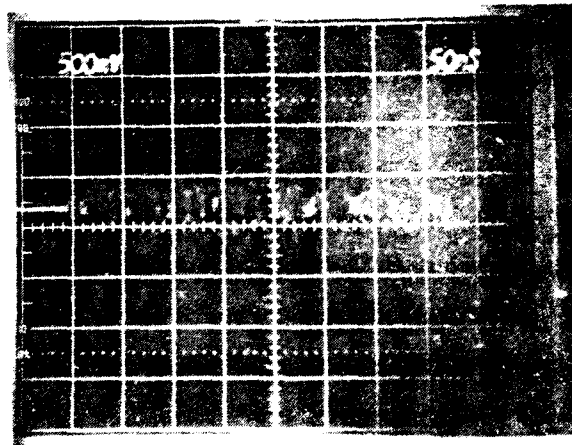
(b) Scope 2, B-dot sensor, 100 cm from front, on center line,  $\theta = 90^\circ$ .

Figure 9. Shot 3 scope photos. In-line attenuation - 5, balun attenuation - 2.



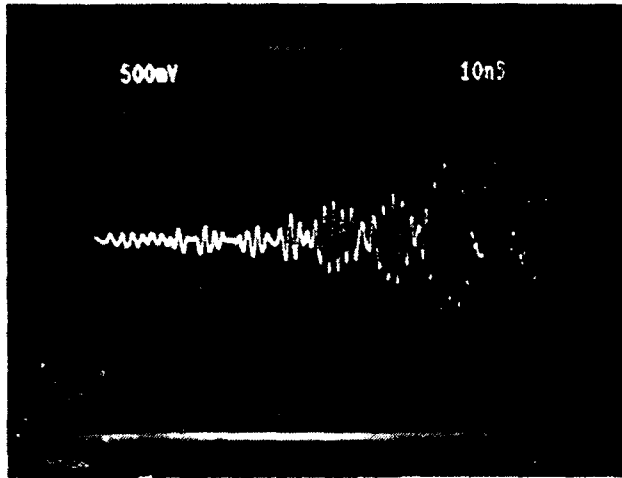
(a) Scope 1, B-dot sensor, 100 cm from front, on center line,  $\theta = 0^\circ$ . Signal split (1&2)  $\sim 2$ .

(b) Scope 2, B-dot sensor, 100 cm from front, on center line,  $\theta = 0^\circ$ . Signal split (1&2)  $\sim 2$ , split again (2&3)  $\sim 1.67$ .



(c) Scope 3, Upper trace, B-dot sensor, 100 cm from front, on center line,  $\theta = 0^\circ$ . Signal split (1&2)  $\sim 2$ , split again (2&3)  $\sim 7.5$ . No lower trace.

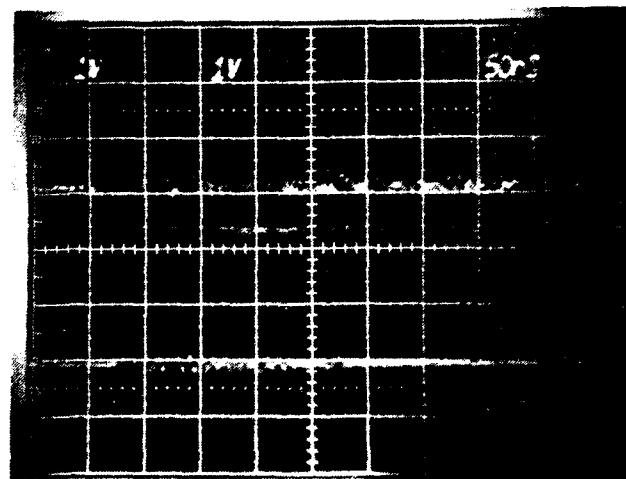
Figure 10 Shot 4 scope photos. Balun attenuation - 2



(a) Scope 1, B-dot sensor, 70 cm from front, on center line,  $\theta = 0^\circ$ . Signal split with 6-dB splitter (1&2) - 2.

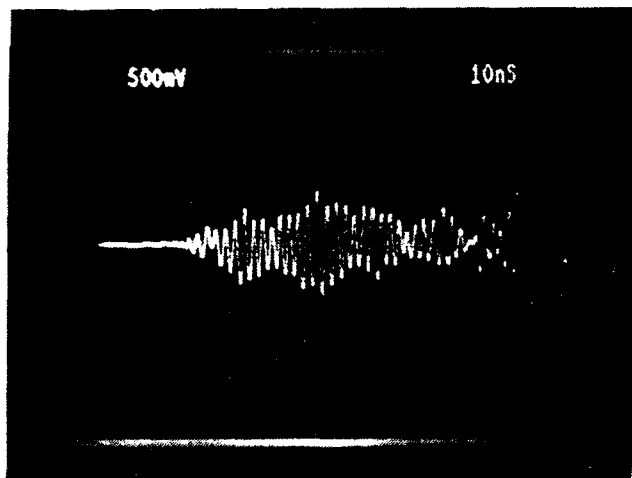


(b) Scope 2, B-dot sensor, 70 cm from front, on center line,  $\theta = 0^\circ$ . Signal split with 6-dB splitter (1&2) - 2.

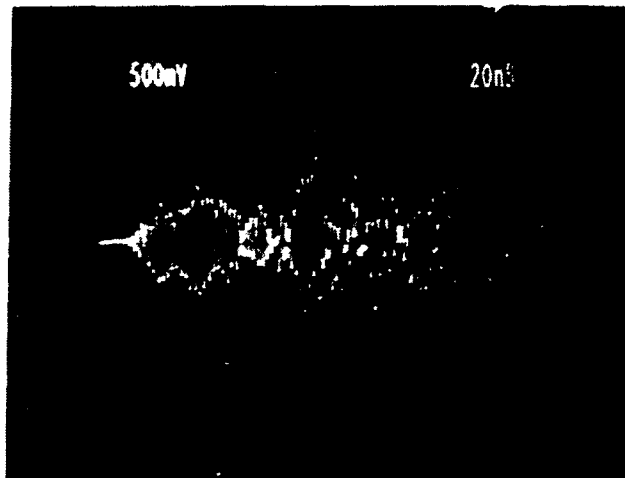


(c) Scope 3. Upper trace - B-dot sensor, 70 cm from front, on center line,  $\theta = 90^\circ$ . In-line attenuation - 5. Lower trace - RG-58 coaxial cable (1 m) with 50- $\Omega$  terminator.

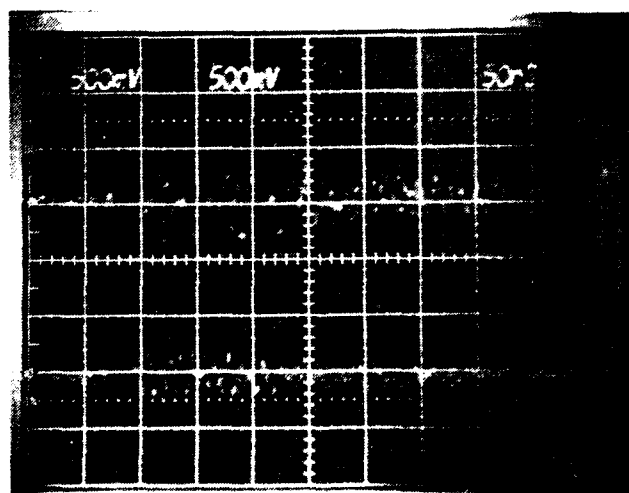
Figure 11. Shot 5 scope photos. Balun attenuation - 2.



(a) Scope 1, B-dot sensor, 70 cm from front, on center line,  $\theta = 0^\circ$ . Signal split with 6-dB splitter (1&2) - 2.

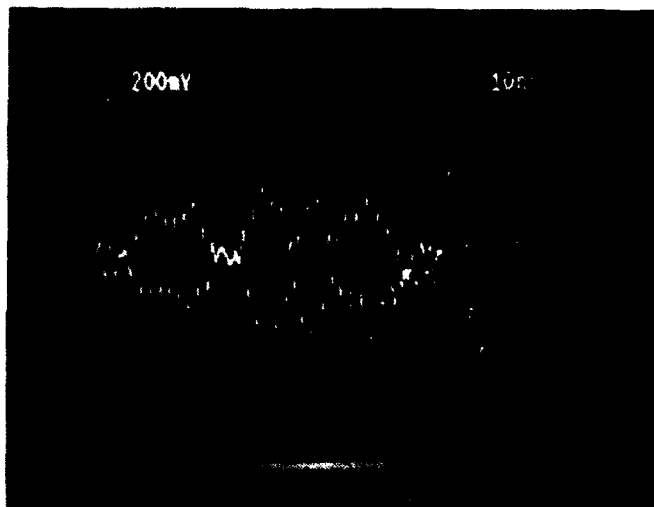


(b) Scope 2, B-dot sensor, 70 cm from front, on center line,  $\theta = 0^\circ$ . Signal split with 6-dB splitter (1&2) - 2.

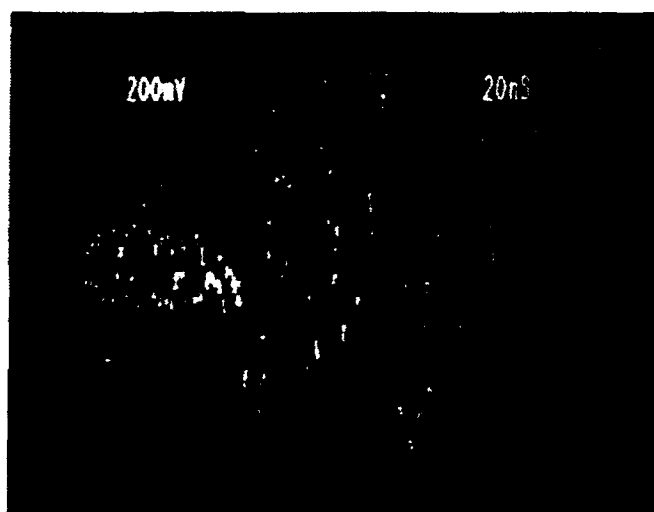


(c) Scope 3. Upper trace - B-dot sensor, 70 cm from front, on center line,  $\theta = 90^\circ$ . In-line attenuation - 5. Lower trace - RG-58 coaxial cable (1 m) with 50- $\Omega$  terminator.

Figure 12. Slot 6 scope photos. Balun attenuation - 2.

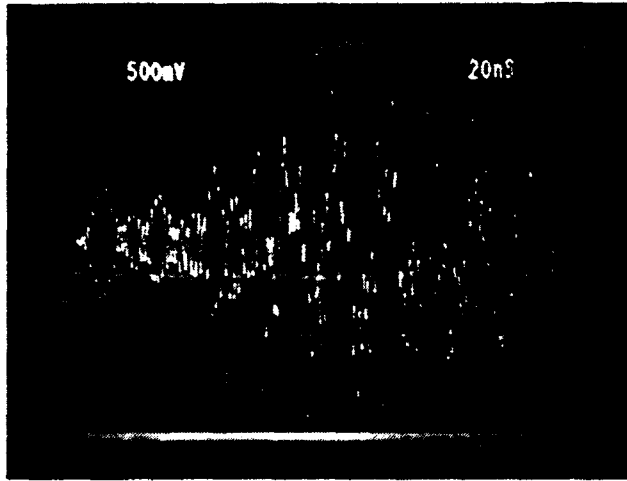


(a) Scope 1, HSD-3 D-dot sensor, 70 cm from front, on center line,  $\theta = 90^\circ$ .

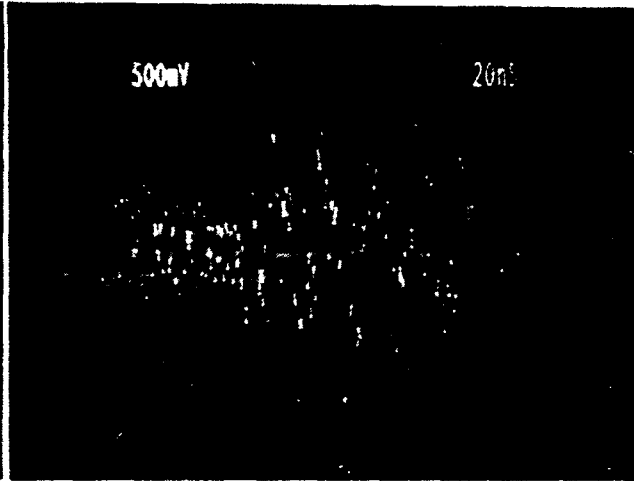


(b) Scope 2, HSD-3 D-dot sensor, 70 cm from front, on center line,  $\theta = 0^\circ$ .

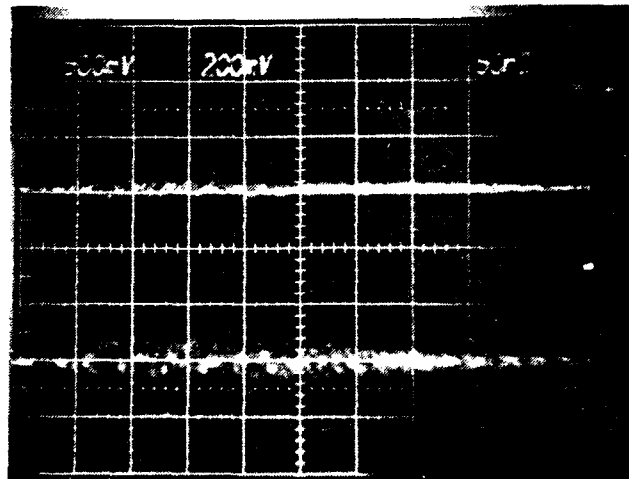
Figure 13. Shot 7 scope photos. In-line attenuation - 25.



(a) Scope 1, HSD-3 D-dot sensor, 70 cm from front, on center line,  $\theta = 90^\circ$ . In-line attenuation - 25.

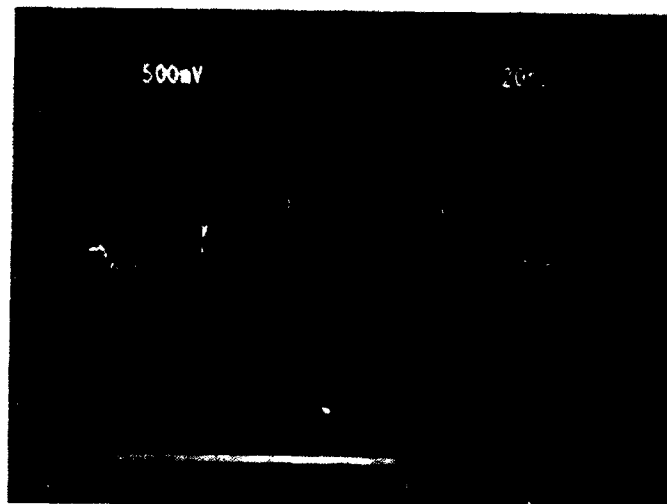


(b) Scope 2, HSD-3 D-dot sensor, 70 cm from front, on center line,  $\theta = 0^\circ$ . In-line attenuation - 25.

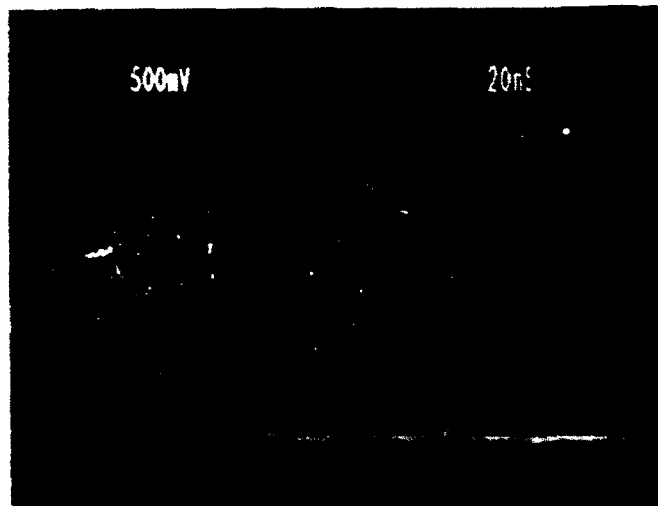


(c) Scope 3, both traces - ACD-4B D-dot sensor, 90 cm from front, on center line,  $\theta = 45^\circ$ . Signal split with 6-dB splitter - 2, in-line attenuation - 50.

Figure 14. Shot 8 scope photos.

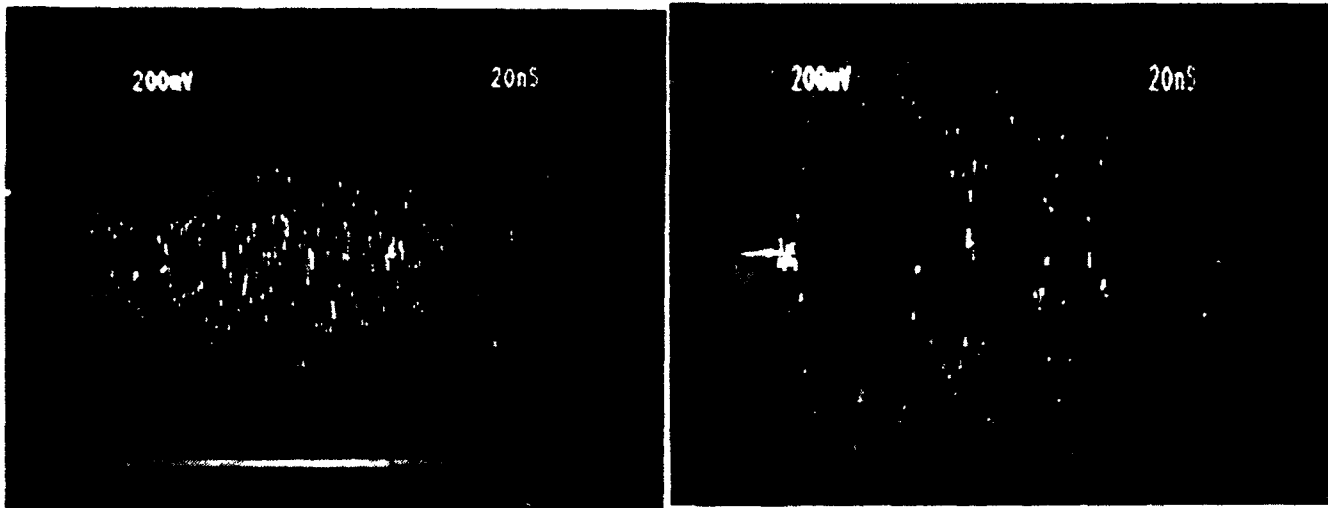


(a) Scope 1, B-dot sensor, 70 cm from front, on center line,  $\theta = 0^\circ$ , signal cables ungrounded.



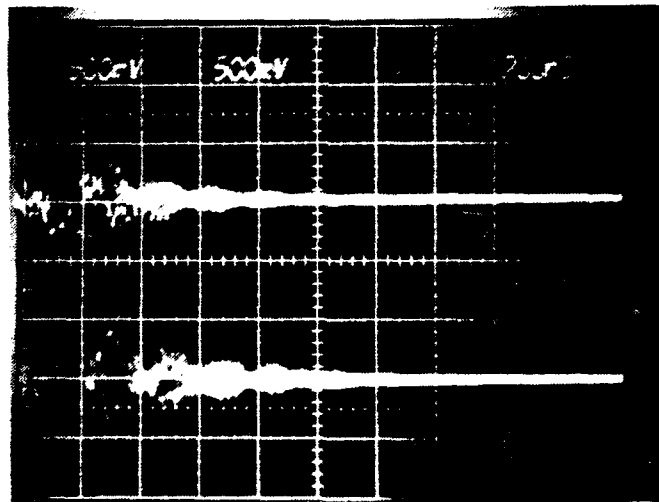
(b) Scope 2, B-dot sensor, 70 cm from front, on center line,  $\theta = 0^\circ$ , signal cables fully grounded.

Figure 15. Shot 9 scope photos. Balun attenuation - 2.



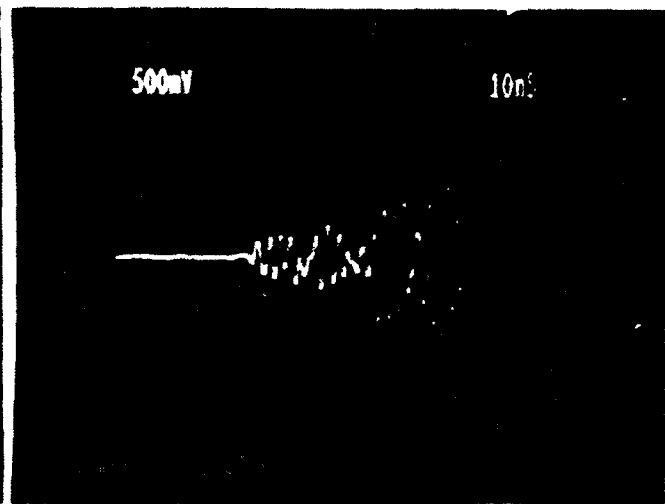
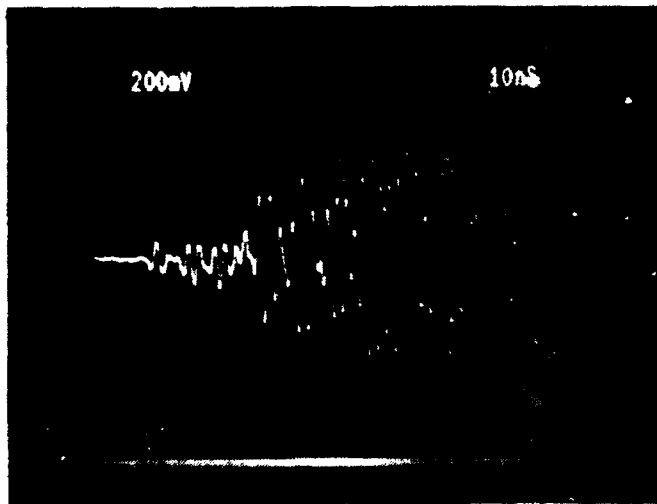
(a) Scope 1. HSD-3 D-dot sensor, 70 cm from front, on center line,  $\theta = 0^\circ$ . Signal split with 6-dB splitter (1&3a) - 2, in-line attenuation - 25.

(b) Scope 2, B-dot sensor, 70 cm from front, on center line,  $\theta = 0^\circ$ . Signal split with 6-dB splitter (2&3b) - 2, balun attenuation - 2.



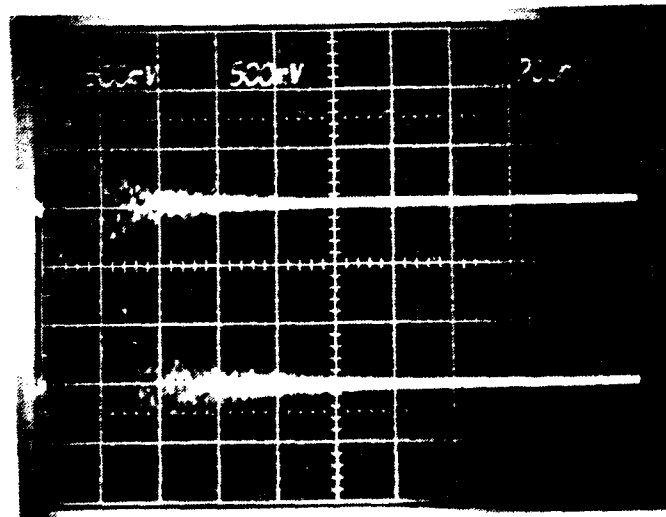
(c) Scope 3. Upper trace - HSD-3 D-dot sensor, 70 cm from front, on center line,  $\theta = 0^\circ$ . Signal split with 6-dB splitter (1&3a) - 2, in-line attenuation - 25. Lower trace - B-dot sensor, 70 cm from front, on center line,  $\theta = 0^\circ$ . Signal split with 6-dB splitter (2&3b) - 2, balun attenuation - 2.

Figure 16. Shot 10 scope photos.



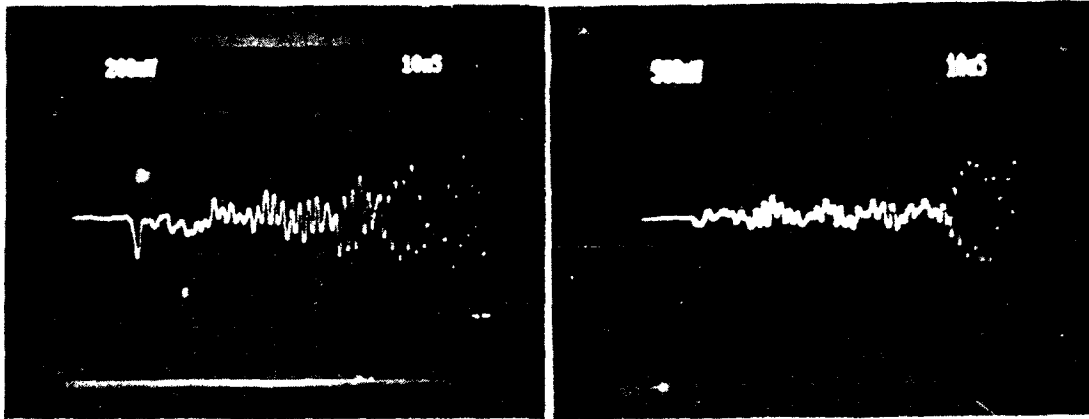
(a) Scope 1, HSD-3 D-dot sensor, 70 cm from front, on center line,  $\theta = 0^\circ$ . Signal split with 6-dB splitter (1&3a) - 2, in-line attenuation - 25.

(b) Scope 2, B-dot sensor, 70 cm from front, on center line,  $\theta = 0^\circ$ . Signal split with 6-dB splitter (2&3b) - 2, balun attenuation - 2.



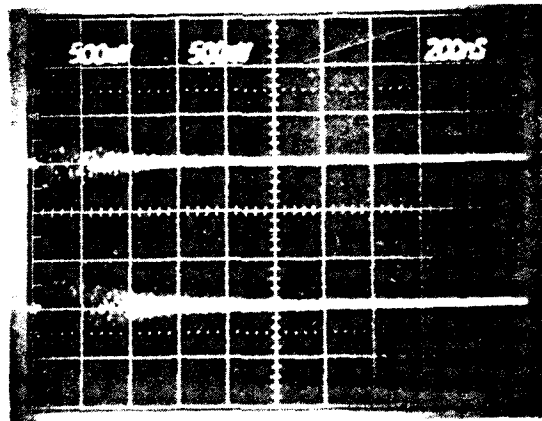
(c) Scope 3. Upper trace - HSD-3 D-dot sensor, 70 cm from front, on center line,  $\theta = 0^\circ$ . Signal split with 6-dB splitter (1&3a) - 2, in-line attenuation - 25. Lower trace - B-dot sensor, 70 cm from front, on center line,  $\theta = 0^\circ$ . Signal split with 6-dB splitter (2&3b) - 2, balun attenuation - 2.

Figure 17. Sheet 11 scope photos.



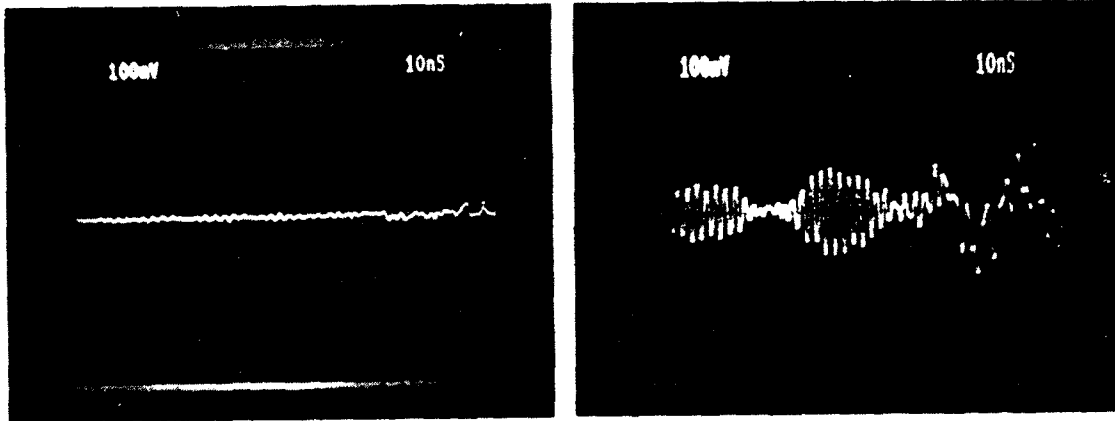
(a) Scope 1, HSD-3 D-dot sensor, 70 cm from front, on center line,  $\theta = 0^\circ$ . Signal split with 6-dB splitter (1&3a)  $\times 2$ , in-line attenuation  $\times 25$ .

(b) Scope 2, B-dot sensor, 70 cm from front, on center line,  $\theta = 0^\circ$ . Signal split with 6-dB splitter (2&3b)  $\times 2$ , balun attenuation  $\times 2$ .



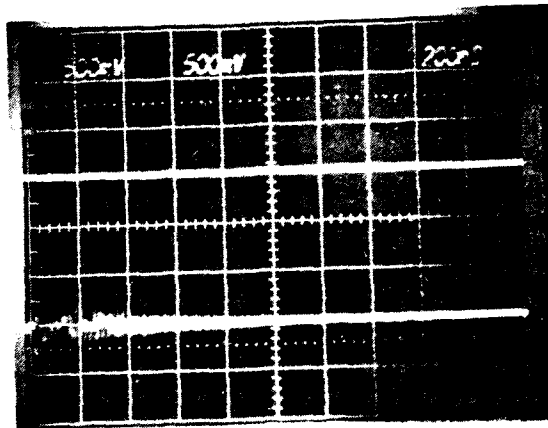
(c) Scope 3, upper trace - HSD-3 D-dot sensor, 70 cm from front, on center line,  $\theta = 0^\circ$ . Signal split with 6-dB splitter (1&3c)  $\times 2$ , in-line attenuation  $\times 25$ . Lower trace - B-dot sensor, 70 cm from front, on center line,  $\theta = 0^\circ$ . Signal split with 6-dB splitter (2&3c)  $\times 2$ , balun attenuation  $\times 2$ .

Figure 18. Screenshot scope photos. The sensors were shielded with a screen (stainless steel, 0.5 mm wire diam., 2.8 mm spacing).



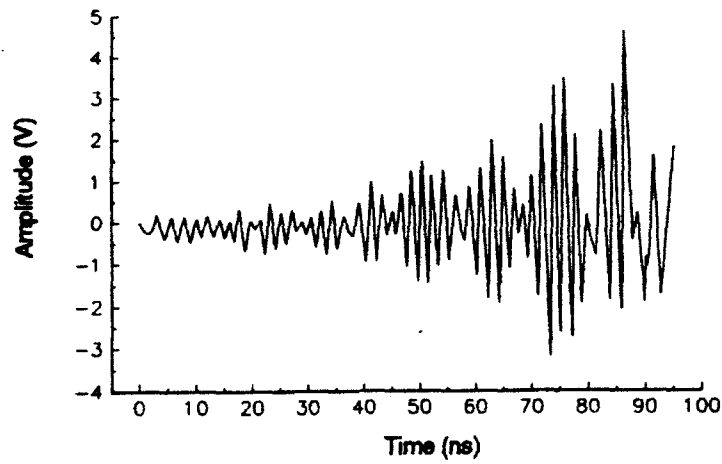
(a) Scope 1, HSD-3 D-dot sensor, 75 cm from front, on center line,  $\theta = 0$ . Signal split with 6-dB splitter (1&3a) - 2, in-line attenuation - 25.

(b) Scope 2, 50- $\Omega$  terminator at BNC connector inside box. In-line attenuation - 5.

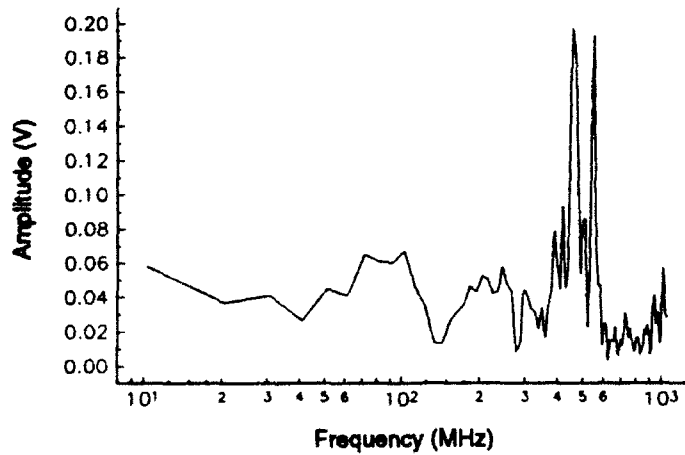


(c) Scope 3. Upper trace - HSD-3 D-dot sensor, 75 cm from front, on center line,  $\theta = 0$ . Signal split with 6-dB splitter (1&3a) - 2, in-line attenuation - 25. Lower trace - B-dot sensor, 75 cm from front, on center line,  $\theta = 0$ . Balun attenuation - 2.

Figure 19 Shot 13 scope photos. The sensors were placed in an aluminum box (3-mm thick, 43 x 43 x 25 cm).

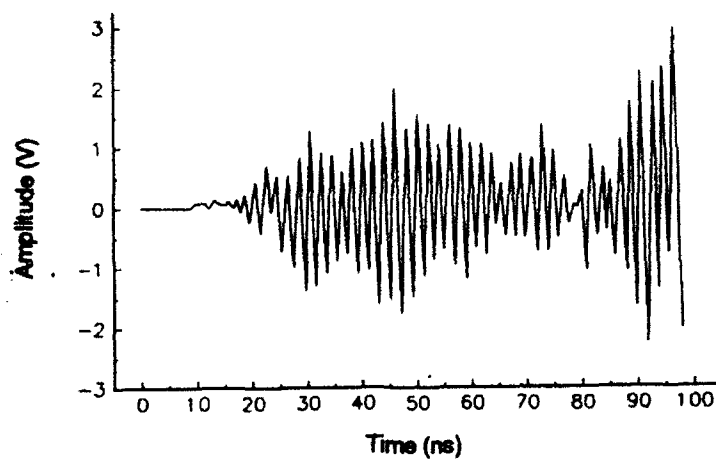


(a) Spectrum of digitized data of scope 1 photo (Fig. 11a).

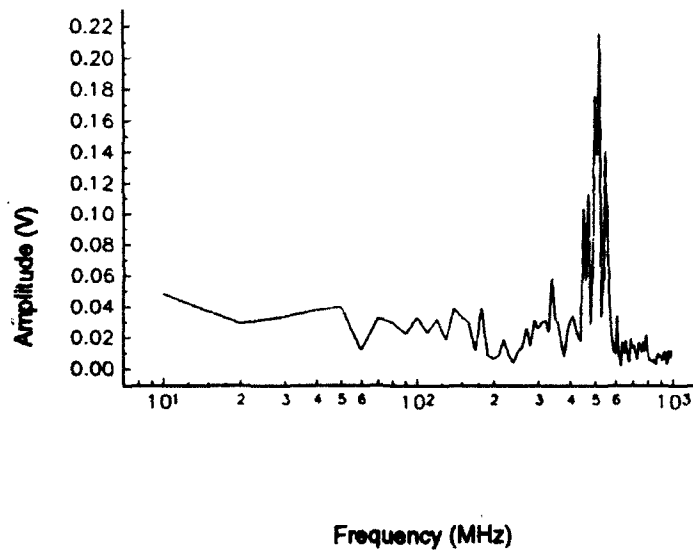


(b) Fourier spectrum of digitized data.

Figure 20. Digitized image and Fourier spectrum of the signal for shot 5.

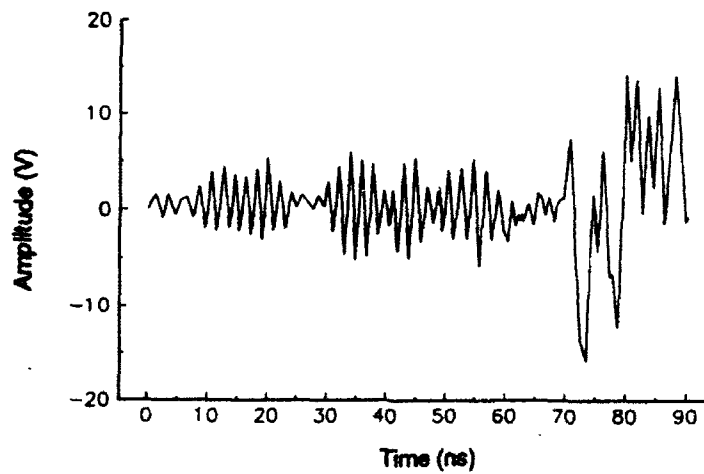


(a) Spectrum of digitized data of scope 1 photo (Fig. 12a).

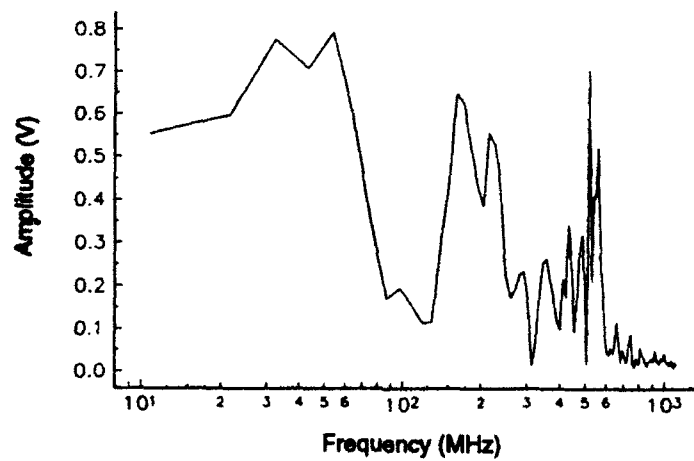


(b) Fourier spectrum of digitized data.

Figure 21. Digitized image and Fourier spectrum of the signal for shot 6.

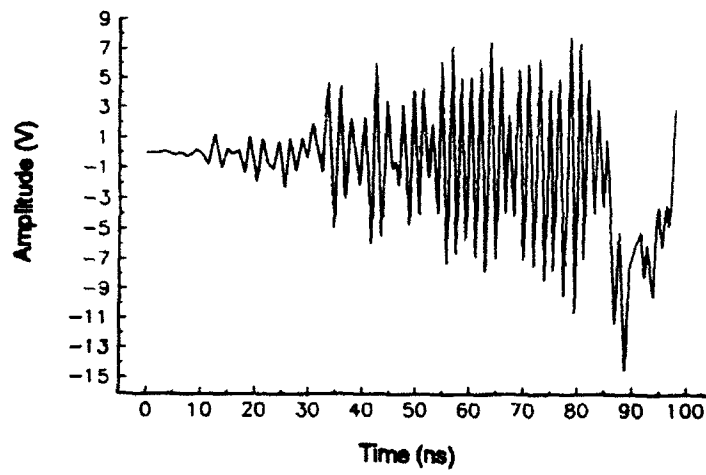


(a) Spectrum of digitized data of scope 1 photo (Fig. 13a).

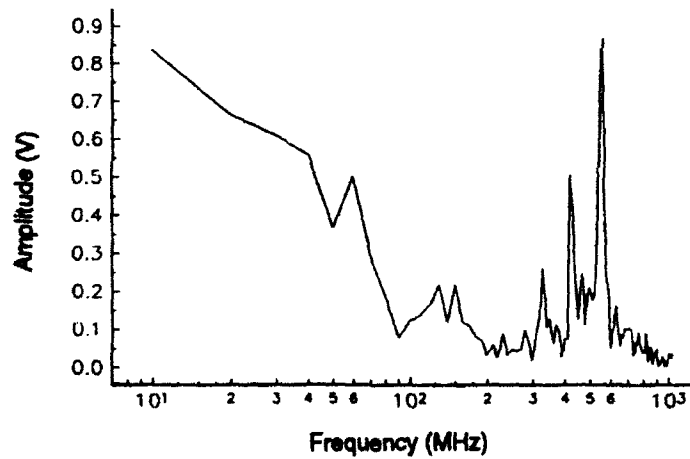


(b) Fourier spectrum of digitized data.

Figure 22. Digitized image and Fourier spectrum of the signal for shot 7.



(a) Spectrum of digitized data of scope 1 photo (Fig. 17a).



(b) Fourier spectrum of digitized data.

Figure 23. Digitized image and Fourier spectrum of the signal for shot 11.

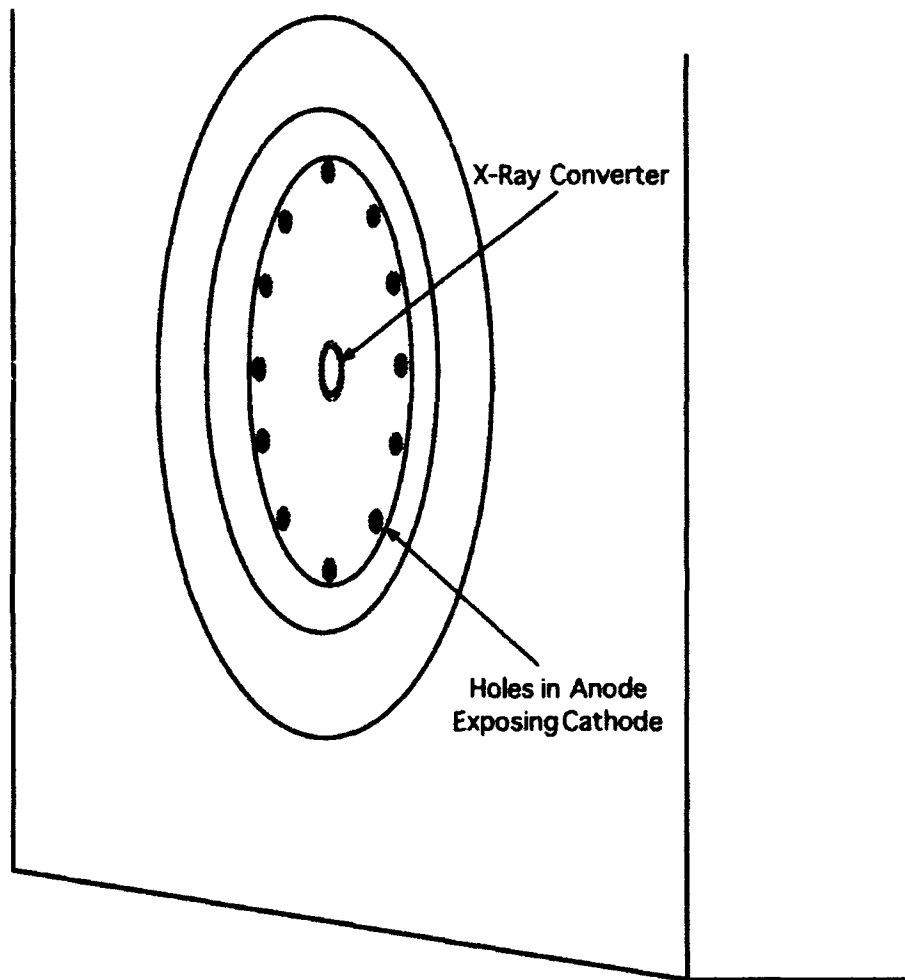


Figure 24. Front end of the SPEED machine showing holes in anode plate that expose cathode plate.

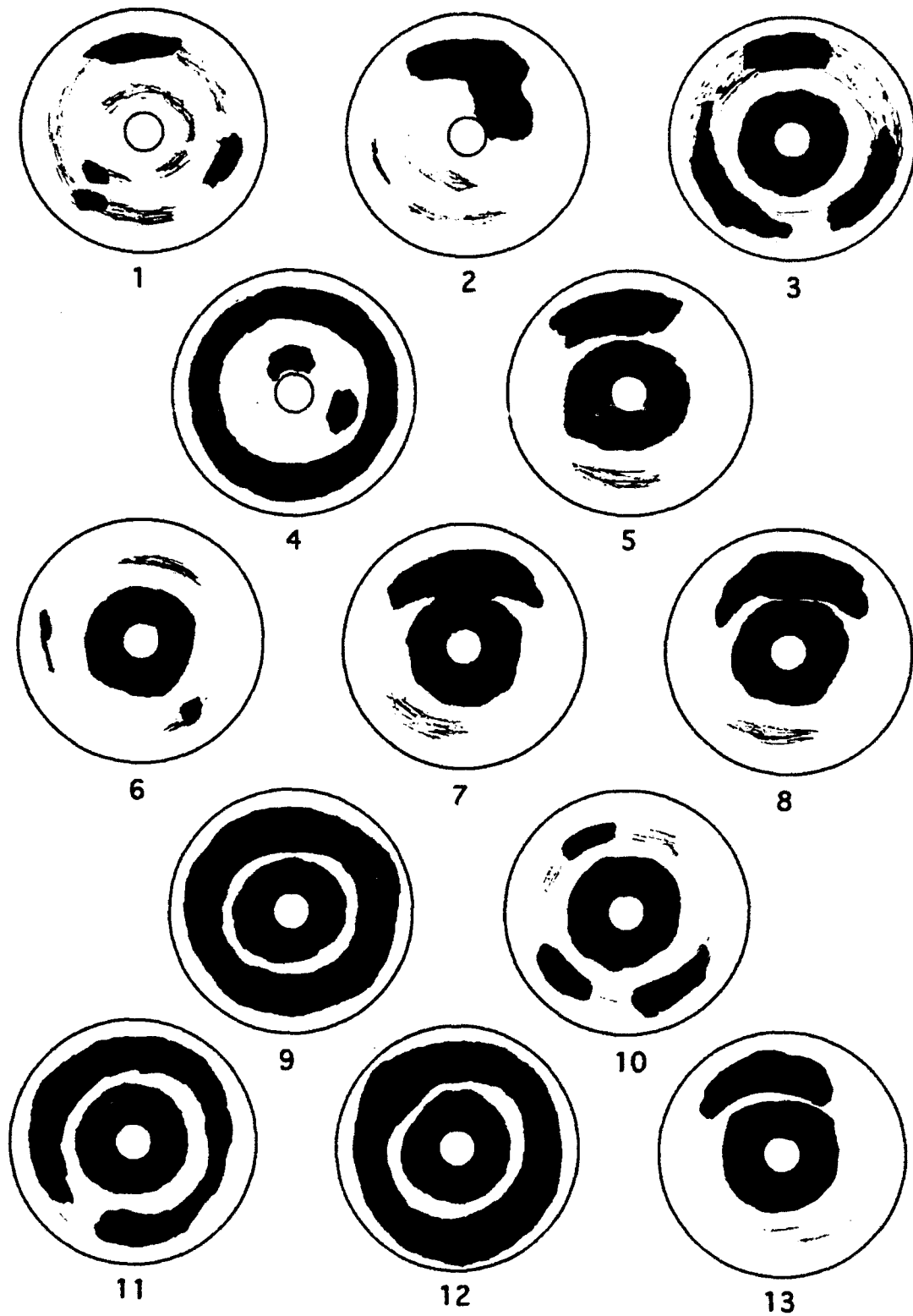


Figure 25. Comparison of tantalum targets for shots 1-13. Black indicates evaporation of the target. Shading indicates some degree of damage.

#### 4.0 RESULTS AND CONCLUSIONS

The following summarizes the results from this experiment:

- For short, unshielded cables connecting electronics to the connectors at the chamber wall, cable-generated currents are  $<5 \text{ mA/m}$ .
- The time derivative of the H-field in the chamber can be detected at all angles, builds to a maximum of  $7.6 \times 10^9 \text{ A/m-s}$  at 100–200 ns, then decays for  $\sim 1000 \text{ ns}$ .
- The time derivative of the E-field in the chamber can be detected at all angles, builds to a maximum of  $9 \times 10^{10} \text{ V/m-s}$  at 100–200 ns, then decays for  $\sim 1000 \text{ ns}$ .
- For sensors located approximately in the center of the chamber, the characteristic frequencies for both the E- and H-fields were approximately 460 and 550 MHz.
- Starting about 100 ns after the pulse, the electrons rebounding between the target and the generators create the largest component of the E-field, with a frequency of  $\sim 60 \text{ MHz}$ .
- During some shots, a significant EM field is generated prior to the trigger of the x-ray pulse.

Damping of resonating EM fields in large cylindrical chambers at facilities designed to simulate an x-ray environment has been studied previously (Refs. 1-8). The following guidelines could be applied to the design and construction of a damper for the SPEED chamber:

- For a sheet damper, the best material impedance is between 200 and 300  $\Omega/\text{square}$  (Refs. 1-4).
- Damper membranes should be placed between 0.7 and 0.9 tank radius (Refs. 1-4).

- A single-sheet membrane rippled between 0.7 and 0.9 tank radius will damp as well as a double-sheet membrane (Refs. 4 and 5).
- If a grid damper (e.g., a screen material) is used, it can be nearly as effective as (but more expensive than) a sheet damper (Refs. 5 and 6). For example, the criterion for a grid damper to obtain a damping rate at least 90 percent of a sheet damper would be

$$0.9 < 1 - \frac{377 d}{\omega \lambda} \left[ \frac{1}{4} + \ln \left( \frac{d}{2\pi a} \right) \right]$$

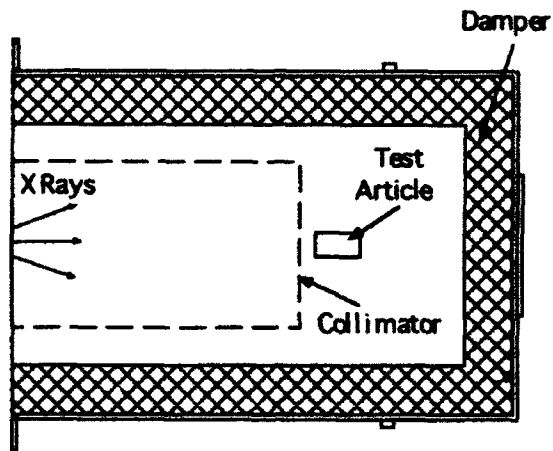
where  $a$  and  $d$  are the radius and separation of the grid wires in meters, respectively,  $\omega$  is the sheet resistance in  $\Omega/\text{square}$ , and  $\lambda$  is the highest frequency wavelength (in meters) of interest.

- Radial sections of damper material extending from the tank wall may be used to damp lower mode responses of the test object and ground the damper to the tank walls. This will eliminate charge buildup effects within the damper (Refs. 5 and 6).

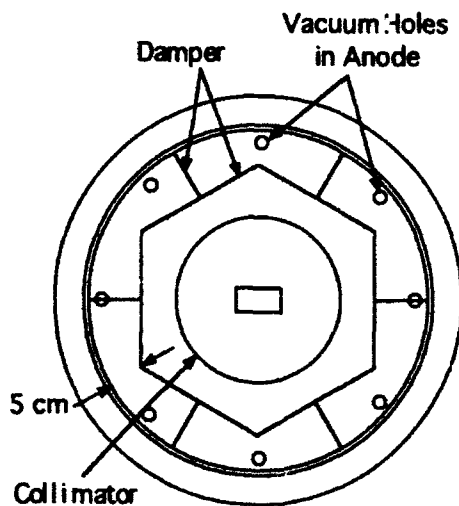
Because of the unique design of the SPEED diode, an additional precaution is recommended for experiments which can not be contained in a faraday shield enclosure (such as the aluminum box used for shot 13):

- The source should be collimated to reduce the area of tank emission (Ref. 4) and reduce direct shine of electrons and EM fields from the vacuum holes in the anode plate.

The configuration for an EM-shielded design of the SPEED chamber using these guidelines is shown in Figure 26. The test object should be placed no closer than 10 cm to the damping material to prevent inductive effects. The effectiveness of such a design should be tested using similar techniques to those employed for this experiment. It is recommended that such tests be performed prior to further experiments of high-frequency-sensitive circuits in an unshielded configuration.



(a) Side view.



(b) End view.

Figure 26. Geometry of a collimator and grounded hexagonal damper for the large SPEED chamber.

## REFERENCES

1. Brown, T.L., Spherical Cavity Resonant Damping Through the Use of an Impedance Loaded Shell Inside the Chamber, AFWL Sensor and Simulation Note 204, July 1, 1974.
2. Tumolillo, T.A. and Wondra, J.P., "SGEMP Simulation Chamber Damping Studies," IEEE Trans. on Nucl. Sci. NS-25, No. 6, December 1978.
3. Dancz, J. and Stettner, R., "On Electromagnetic Environmental Fidelity in Damped Cylindrical Cavities," IEEE Trans. on Nucl. Sci. NS-27, No. 6, December 1980.
4. Goplen, B. et al., "Three-Dimensional SGEMP Simulation of an Idealized FLTSATCOM in SXTF," IEEE Trans. on Nucl. Sci. NS-27, No. 6, December 1980.
5. Seidler, W. et al., "Experimental Evaluation of a Large Grounded Hexagonal Damper and a Ferrite Isolated Data Link for SGEMP Testing," IEEE Trans. on Nucl. Sci. NS-28, No. 6, December 1981.
6. Goldstein, B., Stettner, R., and Schwartz, S., "The Polarization of Resistive Membranes and the Damping Rate of Grid Dampers," IEEE Trans. on Nucl. Sci. NS-27, No. 6, December 1980.
7. Fromme, D.A., Van Lint, V.A., Stettner, R., Macgurn, R.W., and Goldstein, B.M., "Exploding-Wire Photon Testing of SKYNET Satellite," IEEE Trans. on Nucl. Sci. NS-25, No. 6, December 1978.
8. Seidler, W.A. and Neal, W.R., "Experimental Investigations of the Damping of an SGEMP Simulation Chamber Using a Single Sheet Impedance Loaded Damper," IEEE Trans. on Nucl. Sci. NS-24, No. 6, December 1977.

APPENDIX  
EQUIPMENT

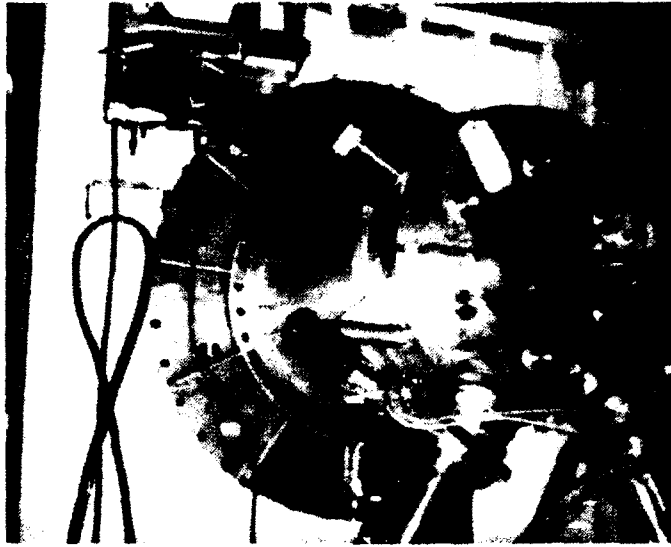


Figure A-1. Large chamber attached to the SPEED machine.

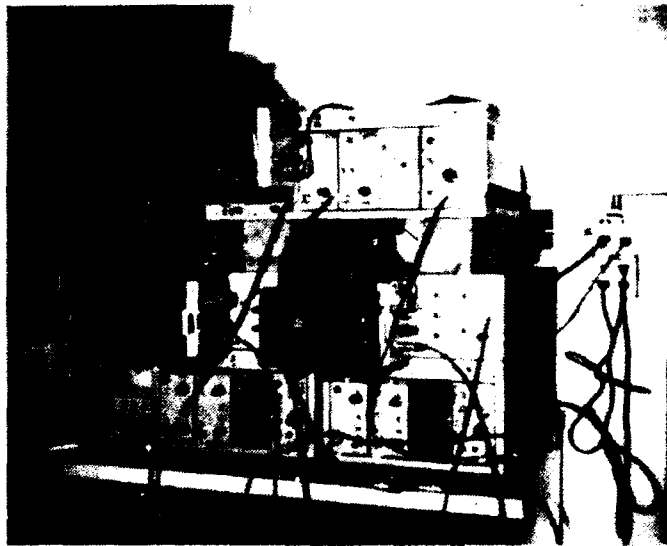


Figure A-2. Camera-equipped oscilloscopes in the shield room.

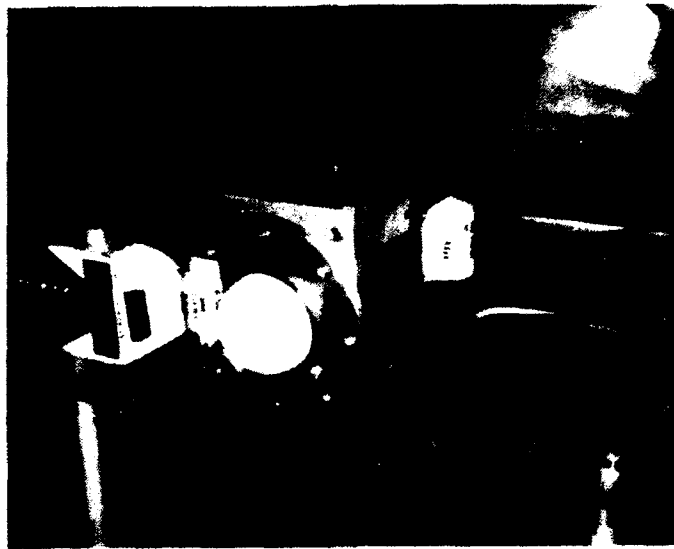
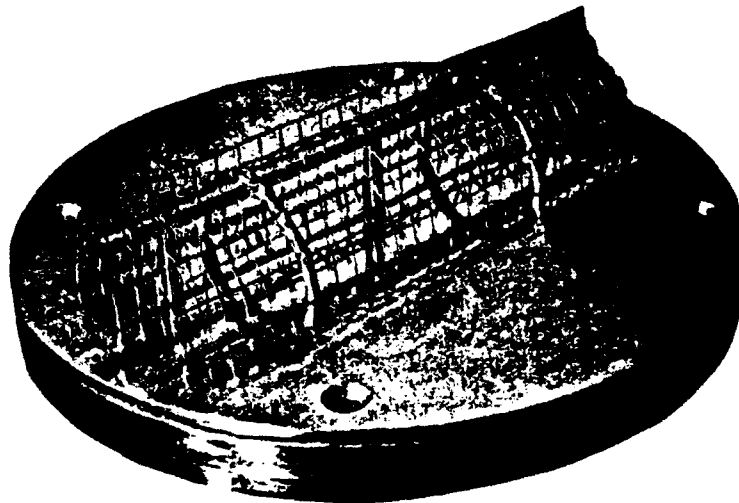


Figure A-3. The D- and B-dot sensors mounted on an aluminum box in the chamber.

EG&G  
Washington Analytical Services Center, Inc.  
2450 Alamo Avenue, SE  
P.O. Box 9100  
Albuquerque, NM 87119

Data Sheet 1109  
September 1980

# CML $\dot{B}$ SENSOR (Ground Plane) (RADIATION HARDENED)



The CML (Cylindrical Moebius Loop) B-dot sensors (Models 3, 5, and 6) are small radiation hardened half cylinder loops mounted on conducting ground plates for positioning on a ground plane to measure the time rate-of-change of an incident magnetic field in a gamma radiation environment. These sensors can also be used for surface current density measurements. These probes are passive devices requiring no external power.

These sensors are cylindrical loops with one gap and the pickoff cables wired in a moebius configuration. The voltage signal developed across the gap by the changing magnetic field is sensed in the differential mode by the pickoff cables. The moebius configuration and the differential output provide for common mode rejection of unwanted signals generated in the cables by the gamma radiation and electric field components. The output cables of all CML sensors exit through the ground plane (radial version), normal to the cylinder axis.

The X-versions of these sensors have the sensing loop structure formed from a sparse wire grid. This maximizes the transparency of the sensor to X-rays and photoelectrons.

## PERTINENT EQUATION

$$V_o = \vec{A}_{eq} \cdot \frac{d\vec{B}}{dt} = \text{sensor output (in volts)}$$

where

$$\vec{A}_{eq} = \text{sensor equivalent area (in m}^2\text{)}$$

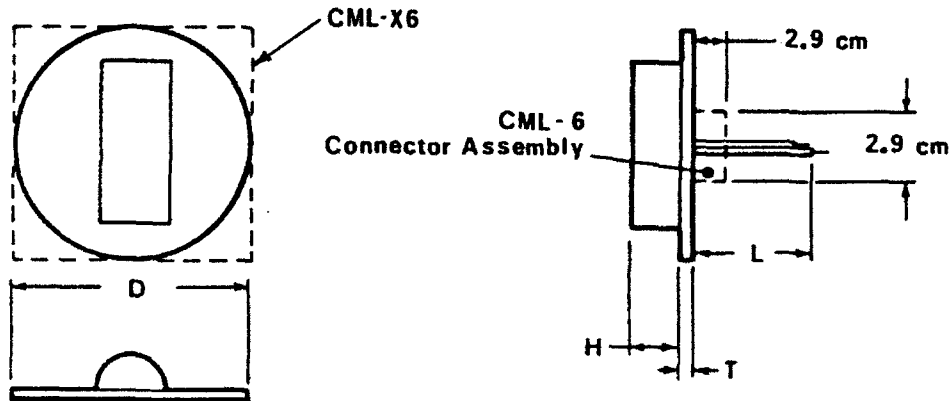
$$\vec{B} = \text{magnetic flux density vector (in teslas)}$$

**SPECIFICATIONS**

Parameter	CML-3	CML-X3	CML-X5	CML-6	CML-X6
Equivalent Area	$5 \times 10^{-4} \text{ m}^2$	$5 \times 10^{-4} \text{ m}^2$	$1 \times 10^{-3} \text{ m}^2$	$5 \times 10^{-3} \text{ m}^2$	$5 \times 10^{-3} \text{ m}^2$
Frequency Response (3dB point)	632 MHz	700 MHz	500 MHz	175 MHz	113 MHz
Risetime	0.6 ns	0.5 ns	0.7 ns	2 ns	3.1 ns
Maximum Output	5 kV peak	1.5 kV* peak	1.5 kV* peak	1.5 kV peak	1.5 kV peak
Maximum Field Change	$1 \times 10^7 \text{ tesla/sec}$	$3 \times 10^6 \text{ tesla/sec}$	$1.5 \times 10^6 \text{ tesla/sec}$	$3 \times 10^5 \text{ tesla/sec}$	$3 \times 10^5 \text{ tesla/sec}$
Radiation Level					
X-ray (< 20 keV)	$10^{11} \text{ rad/sec}$	$10^{13} \text{ rad/sec}$	$10^{13} \text{ rad/sec}$	$10^{13} \text{ rad/sec}$	$10^{13} \text{ rad/sec}$
Y-ray (5 MeV)	$10^{11} \text{ rad/sec}$	$10^{11} \text{ rad/sec}$	$10^{11} \text{ rad/sec}$	$10^{11} \text{ rad/sec}$	$10^{11} \text{ rad/sec}$
Mass	0.736 g	600 g	2400 g	400 g	300 g
Dimensions (cm)					
D	8.69	7.94	15.24	15.24	15.24 square
H	2.032	1.58	2.03	4.50	4.7 w/o cover
T	2.000	1.60	1.60	0.935	0.414
L	up to 2.5m**	up to 2.5m**	up to 2.5m**	2.9 (conn)	3.7 (conn)
Output Connectors	None**	None**	None**	OSM-210-1, 50Ω	OSM-210-1, 50Ω

\* Based on field installation of SMA connectors.  
 \*\* Output cable length is normally 2.5m. Lengths up to 7.5m and connector terminations available upon request.

NOTE: 1) Mass indicated for CML-X3 and CML-X5 includes lead shielding.  
 2) Ground plane thickness noted includes lead shield material thickness.



(Data and Specifications Subject to Change without Notice)

EG&G  
Washington Analytical Services Center, Inc.  
2450 Alamo Avenue, SE  
P.O. Box 9100  
Albuquerque, NM 87119

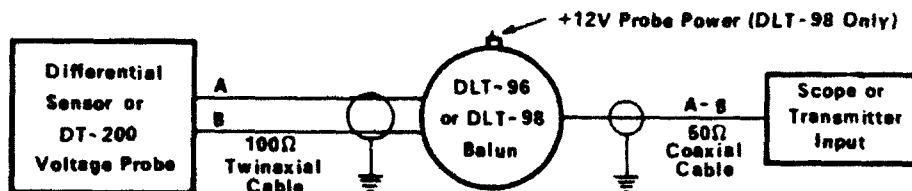
Data Sheet 1300  
September 1980

## DLT-96, 97, 98 BALUNS



Obtaining valid measurements in electromagnetic environments such as in an EMP simulator requires distortion-free instrumentation. The DLT-96 and DLT-98 baluns minimize signal distortion while transforming the balanced signal on a twinaxial cable from a differential EMP field sensor or voltage probe for input to a 50-ohm unbalanced coaxial cable, oscilloscope, or isolated data link (A-B mode). They eliminate the need for twinaxial "Tee" connectors and matched-length coaxial cable pairs. The DLT-98 series performs all the functions of the DLT-96 while also providing the means for supplying dc power to the EG&G DT-200 differential voltage probe (Data Sheet 1320).

The DLT-96A and DLT-98A baluns are shielded for use in fast risetime EMP environments as intense as 100 kV/m. (Noise induced by a 6-ns risetime, 100 kV/m pulse is less than 6 mV peak-to-peak.) The DLT-96B and DLT-98B baluns are specially packaged to mount within EG&G microwave and fiber optics transmitter units.



A summing (A - B) model, the DLT-97, is also available. This model is useful for checking induced noise and cable drive to optimize instrumentation configuration.

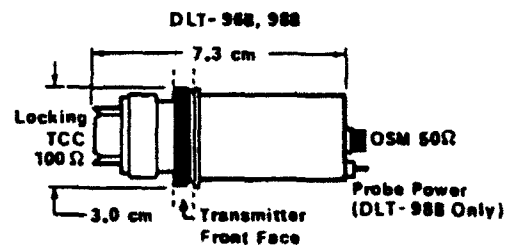
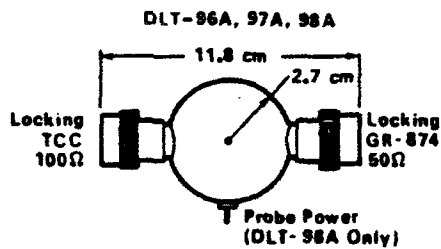
### SPECIFICATIONS

Electrical Specifications:	DLT-96A, B	DLT-97A	DLT-98A, B
<b>Minimum Bandwidth (3-dB Points)</b>			
Upper Limit*	130 MHz	130 MHz	130 MHz
Lower Limit	10 kHz (30 kHz for B)	1 kHz	30 kHz
Bandpass Ripple - $\pm 1$ dB from	40 kHz (120 kHz for B) to 100 MHz	4 kHz to 100 MHz	120 kHz to 100 MHz
<b>Risetime (nominal)</b>	1.3 ns	1.3 ns	1.3 ns
<b>Unbalanced Impedance</b>	50 $\Omega$	50 $\Omega$	50 $\Omega$
<b>Balanced Impedance</b>	100 $\Omega$	100 $\Omega$	100 $\Omega$
<b>Common Mode Rejection**</b> (Minimum anywhere in bandpass)	30 dB	NA	30 dB
<b>Insertion Loss</b>	6 dB	0 dB	8 dB
<b>Signal Level Limits</b>			
Linear Operation (V $\cdot$ $\mu$ s Product)	80	80	40
Peak Signal Protection	$\pm 1$ kV	$\pm 1$ kV	$\pm 1$ kV
<b>Maximum Continuous Power</b>	0.5 watt	0.5 watt	0.5 watt

\*Bandwidth limit extendable to 250 MHz on special order

\*\*25 dB for 250-MHz bandwidth option

#### Physical Dimensions:

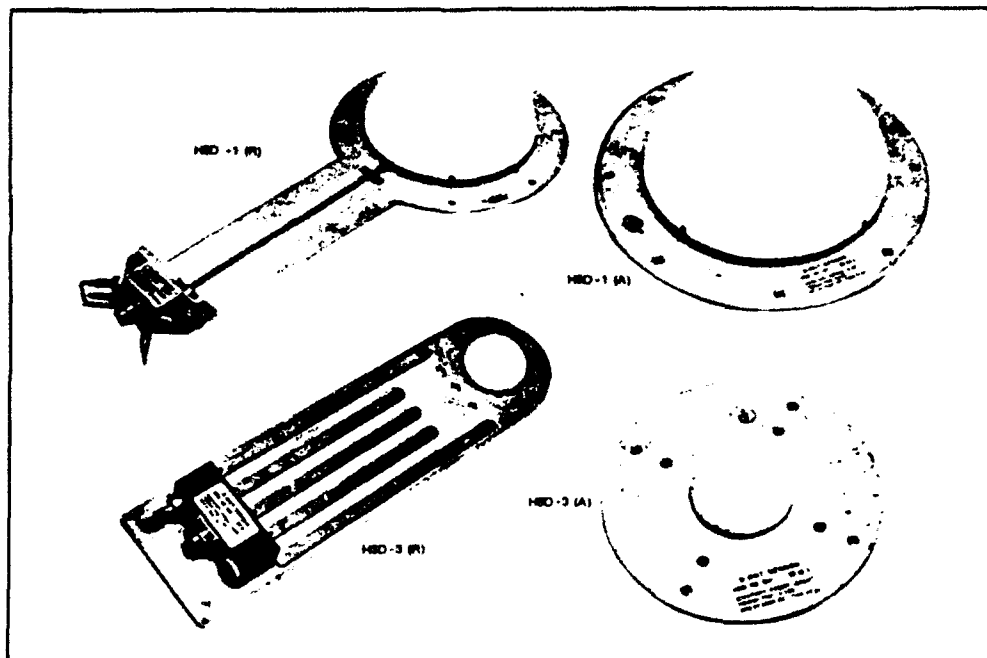


(Data and Specifications Subject to Change without Notice)

EG&G  
Washington Analytical Services Center, Inc.  
2450 Alamo Avenue, SE  
P.O. Box 9100  
Albuquerque, NM 87119

Data Sheet 1115  
September 1980

# HSD $\vec{D}$ SENSORS (Ground Plane)



These HSD (Hollow Spherical Dipole) sensors are mounted on a conducting surface and used to measure the normal component of the displacement current ( $dD/dt$ ). They are used to measure the electric field ( $E = \frac{D}{\epsilon_0}$ ) in numerous EMP simulators such as ALECS and ARES. The HSD can also be used to measure the time rate of change of surface charge density,  $\frac{d}{dt} q_s$ . (Data Sheet 1117 describes special  $\dot{q}_s$  sensors).

These sensors are available in radial and axial configurations with the output connector exiting through the mounting surface in the axial version. The sensor is a passive device and requires no power. Fittings are provided to fill the sensor interior with high dielectric strength gas, such as nitrogen or  $SF_6$ , in high field applications where internal arcing could become a problem.

## PERTINENT EQUATION

$$I_o = \bar{A}_{eq} \cdot \frac{d\bar{D}}{dt}$$

or

$$V_o = R A_{eq} \frac{dD}{dt} \cos \theta$$

where

$I_o$  = sensor output (in amps)

$V_o$  = sensor output (in volts)

$R$  = sensor characteristic load impedance (50 ohms)

$A_{eq}$  = sensor equivalent area (in  $m^2$ )

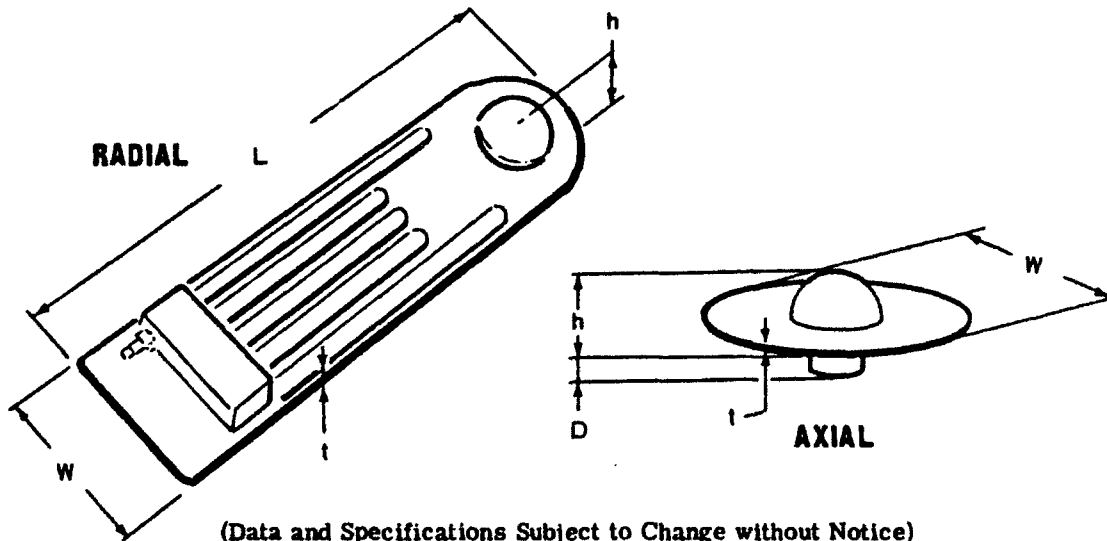
$D$  = magnitude of electric displacement vector ( $\bar{D} = \epsilon_0 \bar{E}$ , in  $Coul/m^2$ )

$\theta$  = angle between  $E$  and vector normal to sensor ground plate

**SPECIFICATIONS**

Parameter	HSD-1		HSD-3	
	Axial*	Radial*	Axial*	Radial*
$A_{eq}$ (m <sup>2</sup> )	1 x 10 <sup>-1</sup>		1 x 10 <sup>-2</sup>	
Frequency Response (3 dB pt)	≥45 MHz		≥150 MHz	
Risetime (T <sub>r</sub> 10-90)	≤7.4 ns		≤2.3 ns	
Maximum Output	5 kV		5 kV	
Output Connector	GR-874L (50Ω)		GR-874L (50Ω)	
Mass	1.8 kg		1.4 kg	
Dimensions (cm)				
L	--	58.4	--	47.0
W	28.2	28.2	17.8	12.7
h	10.4	10.4	3.3	3.3
t	0.32	0.32	0.16	0.16
D	5.8	--	5.8	--

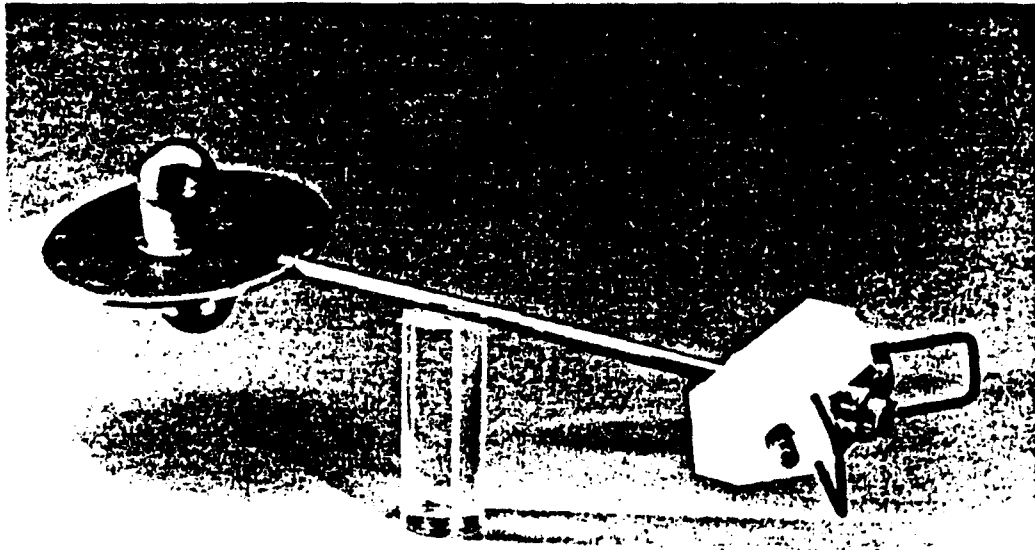
\* Axial or Radial Output Specified by Designations  
HSD-N(A) and HSD-N(R), Respectively where N=1 or 3.



EG&G  
Washington Analytical Services Center, Inc.  
2450 Alamo Avenue, SE  
P.O. Box 9100  
Albuquerque, NM 87119

Data Sheet 1118  
September 1987

# ACD $\dot{D}$ SENSOR (Free Field)



The free - field ACD (Asymptotic Conical Dipole) sensors are used to measure a single component of the displacement current ( $d\vec{D}/dt$ ). The asymptotic cone design exhibits less capacitance than the HSD design and extends the upper frequency limit for the same value of equivalent area ( $A_{eq}$ ). EG&G has developed a shape for the sensing elements which optimizes the bandwidth and pulse response of these sensors.

## PERTINENT EQUATION

$$I_O = \bar{A}_{eq} \frac{d\vec{D}}{dt}$$

or  $V_O = RA_{eq} \frac{dD}{dt} \cos \theta$

where

$I_O$  = sensor output (in amps)

$V_O$  = sensor output (in volts)

$R$  = sensor characteristic load impedance (100 ohms)

$A_{eq}$  = sensor equivalent area (in  $m^2$ )

$D$  = magnitude of electric displacement vector ( $\vec{D} = \epsilon_0 \vec{E}$ , in  $Coul/m^2$ )

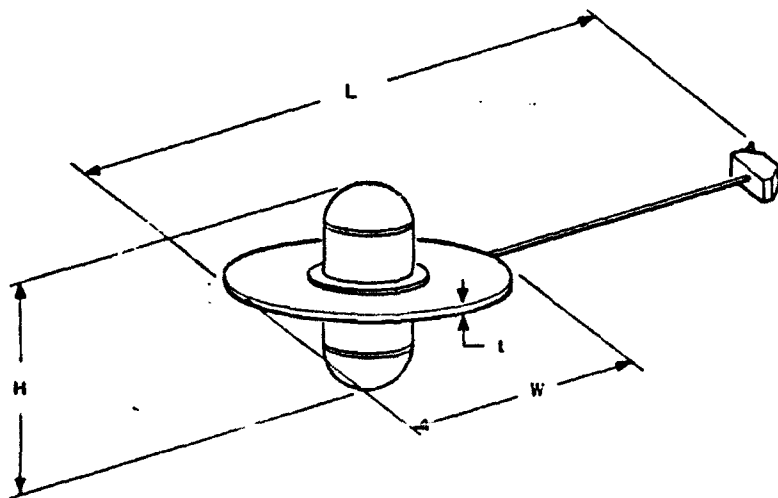
$\theta$  = angle between  $E$  and vector normal to sensor ground plate

### SPECIFICATIONS

	ACD-2(R)	ACD-4(R)	ACD-7(R)	ACD-10(R)
$A_{eq}$ (m <sup>2</sup> )	$1 \times 10^{-4}$	$1 \times 10^{-2}$	$1 \times 10^{-3}$	$1 \times 10^{-1}$
Frequency Response (3 dB point)	>10 GHz	>1.0 GHz	>3.3 GHz	>330 MHz
Risetime ( $T_{r10-90}$ )	<0.033 ns	<0.33 ns	<0.11 ns	<1.1 ns
Maximum Output	125 V	5 kV**	250 V	5 kV**
Output Connector	Dual SMA	TCC-100Ω*	Dual SMA	TCC-100Ω*
Mass (nominal)	30 g	780 g	120 g	2.6 kg
Dimensions (cm)				
L	11.12	49.53	18.50	62.20
W	2.54	13.97	6.50	28.20
H	1.12	9.96	3.30	31.12
t	0.20	0.32	0.25	0.64

\* 100-ohm Twinaxial Connector (EG&G Data Sheet 1340)

\*\* when filled with SF<sub>6</sub>; 2 kV otherwise



(Data and Specifications Subject to Change without Notice)